Solid State NMR Studies of Energy Conversion and Storage Materials

by

Jankuru Hennadige, Sohan Roshel De Silva

A dissertation submitted to the Graduate Faculty in Physics in partial fulfillment of the requirement for the degree of Doctor of Philosophy, The City University of New York

2011

This manuscript has been read and accepted for the Graduate Faculty in Physics in satisfaction of the dissertation requirement for the degree of Doctor of Philosopy.

Prof. Steve G. Greenbaum

August 23, 2011

Date

Chair of Examing Committe

Prof. Igor L. Kuskovsky

August 23, 2011

Date

Executive Office

Prof. Frank Owens

Dr. Thomas B. Reddy

Prof. Sophia N. Suarez

Supervisory Committe

THE CITY UNIVERSITY OF NEW YORK

Abstract

Solid State NMR Studies of Energy Conversion and Storage Materials

by

Jankuru Hennadige, Sohan Roshel De Silva

Advisor: Prof. Steven G Greenbaum

NMR (Nuclear magnetic resonance) spectroscopy is utilized to study energy conversion and storage materials. Different types of NMR techniques including Magic Angle Spinning, Cross-polarization and relaxation measurement experiments were employed. Four different projects are discussed in this dissertation. First, three types of CF_x battery materials were investigated. Electrochemical studies have demonstrated different electrochemical performances by one type, delivering superior performance over the other two. ^{13}C and ^{19}F MAS NMR techniques are employed to identify the atomic/molecular structural factors that might account for differences in electrochemical performance among different types. Next as the second project, layered polymer dielectrics were investigated by NMR. Previous studies have shown that thin film capacitors are improved by using alternate layers of two polymers with complementary properties: one with a high breakdown strength and one with high dielectric constant as opposed to monolithic layers. ^{13}C to ^{1}H cross-polarization techniques were used to investigate any inter-layer properties that may cause the increase in the dielectric strength. The third project was to study two types of thermoelectric materials. These samples were made of heavily doped phosphorous and boron in silicon by two different methods: ball-milled and annealed. These samples were investigated by NMR to determine the degree of disorder and obtain insight into the doping efficiency. The last ongoing project is on a lithium-ion battery system. The nature of passivating layers or the solid electrolyte interphase (SEI) formed on the electrodes surface is important because of the direct correlation between the SEI and the battery life time/durability. Multinuclear (^{7}Li, ^{19}F, ^{31}P) techniques are employed to identify the composition of the SEI formation of both positive and negative electrodes.

Acknowledgements

First of all I would like to give my sincere thanks to my graduate supervisor, Prof. Steven G Greenbaum, who accepted me as a Ph.D. student for his lab without any hesitation. Thereafter, he offered me enormous advice, patiently supervising me, and always guiding me in the right direction. This dissertation would not have been possible without this help and direction.

Special thanks are given to Dr. Phillip Stallworth for introducing me to experimental NMR and always being willing to help me with any experiment NMR issue I had encountered. Also, I am grateful to Prof. J. R. P. Jayakody for assisting me to enter the CUNY Ph.D. program and for his encouragements which made me feel confident.

I also appreciate my 2^{nd} exam committee members, Dr. Thomas B. Reddy and Dr. Sophia Suarez for critical comments, which enabled me to make necessary improvements according to their comments.

I would like to convey my warm thanks to my colleagues and friends: Dr. NKAC Kodiweera, who had helped me in numerous ways from my arrival in the United States through the qualifying exams, Rafael Vazquez for being a brother-like friend. Dr. Paul Sideris, Dr. Nicole Leifer, Jaime Farrington, Sufia Khatan, Victor Udinwe, Marc Berman and Laura Sermasan for being friends and making my graduate life joyful.

I am very greatful to my father, Hemachandra De Silva and mother, Lanka Jayasooriya. They always let me know that they are proud of me, which motivates me to do my best. Their understanding and love encouraged me to work hard and continue pursuing a Ph.D. abroad. I owe my every achievement to both of them.

Last but not least, I am greatly indebted to my devoted wife, Shayami Dickovita and my daughter, Sheneli De Silva for being with me every moment sharing my happiness and sorrow. Their love and support without any complaint or regret has enabled me to complete this Ph.D thesis.

Contents

List of Tables

List of Figures

Chapter 1

Introduction

Since the invention of the first Voltaic pile in 1800 by Alessandro Volta, the battery has become a common power source for many household and industrial applications. According to statistics, the estimated US battery demand in 2012 will be $17 billion with 6% of annual growth[17]. Industry experts are expecting new developments and breakthroughs to fulfill the increasing demand due to theoretical and practical limitations of conventional battery technologies and materials. Investigation of the properties and the arrangement of battery materials are necessarily important for performance improvements and many techniques have been employed for such kind of investigations.

Nuclear magnetic resonance spectroscopy, most commonly known as NMR spectroscopy, is a research technique that exploits the magnetic properties of certain atomic nuclei to determine physical and chemical properties of atoms or the molecules in which they are contained. It relies on the phenomenon of nuclear magnetic resonance and can provide detailed information about the structure, dynamics, reaction state, and chemical environment of molecules. NMR plays a major role in regard to this because of its nuclei specific sensitivity for studying different chemical isotopes which may be used to directly examine these species that are involved in the working battery. The NMR spectrum is sensitive to a number of physical parameters that are related to a working cell/battery such as Li-ion mobility, electronic conductivity and changes of electronic structure of the cations of a redox[1] process. Moreover the integrated individual peaks of a NMR spectrum are proportional to the respective number of active nuclei and which is a quantitative analysis of the environment of the nucleus that is being been probed. That is very important to study the nature and amount of

---

[1] Described in the battery chapter

different compounds (ex. LiF) in a battery with different depth of discharges.

Different projects related to energy technology, in which NMR spectroscopy was utilized are discussed in this thesis:

1. Electrochemically discharged CF_x
2. Layered polymer dielectrics
3. Thermoelectric (TE) Si/B and Si/P alloys
4. Electrolyte breakdown products in the SEI of Li Ion batteries

Chapter 2

Batteries

2.1 Battery fundamentals

An electrochemical battery is a device in which the reaction between two substances can be made to occur in such a way that some of the chemical energy is converted to useful electricity. Although the term "battery" is often used, more precisely the basic electrochemical unit being referred to is the "cell". A battery is a combination of one or more cells, connected in series or parallel or both depending on the voltage and capacity requirement. For example, a 1.5-volt AAA battery is a single 1.5-volt cell, and a 9-volt battery has six 1.5-volt cells in series[18] as shown in Fig. 2.1.1. There are two types of batteries: primary and secondary batteries.

Figure 2.1.1: Three different kinds of 9-volt battery internals.

Primary batteries (also referred to as disposable batteries) produce current immediately on assembly and are intended to be used once and discarded. These are most commonly used in portable devices that have low current drain, used intermittently and used well away from an alternative power source, such as in alarm and communication circuits where other electric power is only intermittently available. Since the chemical reactions are not easily reversible and active materials may not return to their original forms, disposable primary cells cannot be reliably recharged. Zinc-carbon batteries and alkaline batteries are common types in this category.

Secondary batteries (also referred to as rechargeable batteries) must be charged before use and they are usually assembled with active materials in the discharged state. Rechargeable batteries or secondary cells can be recharged by applying electric current, which reverses the chemical reactions that occur during its use. Devices to supply the appropriate current are called chargers or rechargers. There is a vast number of battery types in the rechargeable category such as lead-acid and Li-ion battery types.

2.2 Operation of a cell

A cell consists of three major components. The anode or the negative electrode gives up electrons to the external circuit and is oxidized during the electrochemical reaction. The cathode or the positive electrode accepts electrons from the external circuit. The electrolyte acts as an ionic conducting medium which provides the transfer of charge (ions) inside the cell between anode and cathode. Typically a liquid electrolyte is a solution of a solvent such as water, EC and EMC[1] with dissolved salt ($LiPF_6$, $LiAsF_6$, etc...) in it. Some cells use two half-cells with different electrolytes. A separator between half cells allows ions to flow, but prevents mixing of the electrolytes.

---

[1] EC: Ethyl carbonate, EMC: Ethyl methyl carbonate

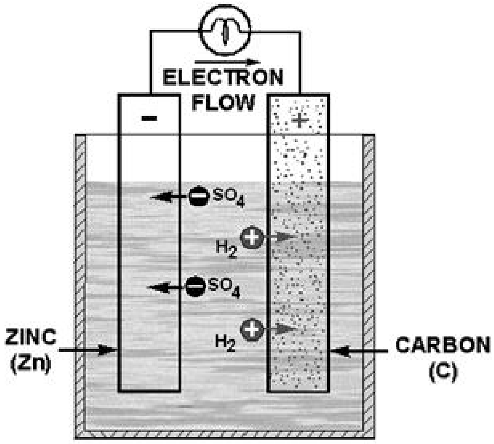

Figure 2.2.1: Simple Galvanic Cell.

If a load is connected externally to the electrodes of a cell, electrons will flow under the influence of a difference in potential across the electrodes from the anode through the external conductor to the cathode. This process is called electrochemical oxidation-reduction[2] (redox) reaction.

The voltage across the electrodes depends primarily upon the materials from which the electrodes are made and to a lesser extent the composition of the electrolyte. The current that a cell delivers depends upon the resistance in the entire circuit, including the cell itself. The internal resistance of the cell depends upon the size the electrodes, the distance between them in the electrolyte, and the resistance of the electrolyte.

The theoretical voltage/potential of a cell is determined by the type of the active material used in the cell and calculated from free-energy data. The decrease in the Gibbs free-energy[3] of a chemical reaction is given by,

$$\triangle G^0 = -nFE^0 \tag{2.2.1}$$

Where F is the Faraday constant ($\sim$ 96,500 C or 26.8 Ah), n is the number of electrons per mole of product and E^0 is the standard electrode potential of the reaction. Standard electrode potentials of some active materials are listed in Table 2.1.

---

[2] The oxidant (oxidizing agent) is a substance that removes electrons from another substance i.e. it oxidizes other substances, and is thus itself reduced. And, because it "accepts" electrons, it is also called an electron acceptor.

[3] (Gibbs) Free-energy is a thermodynamic parameter that measures the "useful" or process-initiating work obtainable from a thermodynamic system at a constant temperature and pressure.

Material	Atomic or molecular mass, g	Standard reduction potential at 25 ^{0}C, V	Valence change
Li	6.94	-3.01	1
Na	23.0	-2.71	1
Mg	24.3	-2.38	2
Al	26.9	-1.66	3
Fe	55.8	-0.44	2
Zn	65.4	-0.76	2
Cl_2	71.0	1.36	2
MnO_2	86.9	1.28	1
Li_xCoO_2	98	1.25	0.5

Table 2.1: Characteristics of typical electrode materials (courtesy of Linden's Handbook of Batteries, fourth edition by Thomas B. Reddy and David Linden).

The cell voltage E^0 can be calculated as,

$$\text{Cell potential} = \text{Anode (oxidation)} + \text{Cathode (reduction)} \tag{2.2.2}$$

Therefore, for example, the standard cell potential of $Zn + Cl_2 \rightarrow ZnCl_2$ will be,

$$\text{Standard potential} = -\left(-0.76V\right) + 1.36V = 2.12V \tag{2.2.3}$$

Although the theoretical cell voltage is calculated in this manner, the practical voltage depends on some other factors such as temperature and conductivity of the electrode materials and electrolyte.

The theoretical capacity of a cell is a measure of the total quantity of electricity involved in the electrochemical reaction of the cell. It is determined by the amount of active material in the cell and defined in terms of Ah (ampere-hours). Theoretical capacity of a Zn/Cl_2 cell can be calculated by the equivalent mass of reactants. Theoretically, 1 gram equivalent mass of active material will deliver 26.8 Ah. Since two electrons are involved and the molecular mass is 65.4 of Zn, the electrochemical equivalent will be,

$$\text{Electrochemical equivalent of Zn} = \frac{65.4g}{26.8Ah \times 2} = 1.22g/Ah \tag{2.2.4}$$

Similarly for the cathode (Cl_2), where molecular mass is 71.0g and electron involvement is 2, will be,

$$\text{Electrochemical equivalent of Cl} = \frac{71.0g}{26.8Ah \times 2} = 1.32g/Ah \tag{2.2.5}$$

Therefore the total theoretical capacity of a Zn/Cl will be $1.22g/Ah + 1.32g/Ah = 2.54g/Ah$ or $0.394Ah/g$.

The energy of a battery is also related to the capacity. The voltage and the current of the battery are considered and the theoretical value is the maximum value that can be delivered by a system. For a Zn/Cl cell, from the calculated potential and the theoretical capacity, the specific energy can be calculated as follows,

$$\text{Specific energy} = 2.12V \times 0.394Ah/g = 835Wh/kg \tag{2.2.6}$$

Although the above mentioned cell operations are general, there are a number of battery chemistries available today. A brief description of Lithium primary and lithium-ion secondary batteries is given in the following section as they are more related to the projects discussed in this thesis.

2.3 Lithium primary batteries

The term "lithium battery" refers to a family of different chemistries, comprising many types of cathodes and electrolytes along with a lithium anode. Lithium metal is very attractive in the battery industry because of its outstanding features such as light weight, being the lightest of all the metallic elements, high voltage and good conductivity. Lithium is preferred to the other alkali metals because of its better mechanical characteristic and lower reactivity. Depending on the cathode material used, a lithium battery can have voltage up to about 4 V. This reduces the number of cells in a battery pack, compared to the 1.5V primary batteries. Many lithium batteries perform over a wide range of temperature 70 to -40 ^{0}C and some are designed to deliver high current and power levels. Lithium batteries also have a superior shelf life, i.e those can be stored for a long period of time.

Nonaqueous solvents for electrolytes are used in lithium batteries. Water in any aqueous solution can react vigorously with lithium, releasing hydrogen and forming lithium hydroxide.

$$2Li + 2H_2O \rightarrow 2LiOH + H_2$$

Organic solvents such as EC (Ethylene carbonate) and PC (Propylene carbonate) or inorganic solvents such as thionyl-chloride are typically used with a salt like $\mathrm{LiPF_6}$. Lithium primary batteries can be categorized in to several types based upon the cathode and the electrolyte listed in Table 2.2 and will not be discussed in detail here.

System	Cathode	Solvent / Solute / Separator	Nominal voltage, V / Specific energy, Wh/kg
$\mathrm{Li/SOCl_2}$	$\mathrm{SOCl_2}$ with carbon	$\mathrm{SOCl_2}$ / $\mathrm{LiAlCl_4}$ / Glass	3.6 / 275
$\mathrm{Li/SO_2Cl_2}$	$\mathrm{SO_2Cl_2}$ with carbon	$\mathrm{SO_2Cl_2}$ / $\mathrm{LiAlCl_4}$ / Glass	3.95 / 480
$\mathrm{Li/CF}_x$	CF_x with carbon on nickel collector	PC+DME / $\mathrm{LiBF_4}$ or $\mathrm{LiAsF_6}$ / Polypropylene	3.0 / 350 or 800
$\mathrm{Li/MnO_2}$	$\mathrm{MnO_2}$ with carbon	PC+DME / Li salt / Polypropylene	3.0 / 230

Table 2.2: Characteristics of some Lithium primary batteries (courtesy of Linden's Handbook of Batteries, fourth edition by Thomas B. Reddy and David Linden).

2.4 Lithium Ion-batteries

A lithium-ion battery is a family of rechargeable battery types in which lithium ions move from the negative electrode to the positive electrode during discharge, and back when charging. Unlike lithium primary batteries, lithium-ion electrochemical cells use an intercalated lithium compounds as the electrode material instead of metallic lithium. Lithium ion batteries are available in wide variety of shapes and sizes efficiently fitting the device they power and much lighter than other comparable secondary batteries. Moreover one of the major advantages is that no memory effect is associated with lithium-ion batteries.

Depending on materials choices, the voltage, capacity, life, and safety of a lithium-ion battery can change dramatically. The anode of a conventional lithium-ion cell is made from carbon. The most commercially popular anode material is graphite. The cathode is a metal oxide usually a layered oxide (such as lithium cobalt oxide), a polyanion (such as lithium iron phosphate), or a spinel (such as lithium manganese oxide)[19]. These materials are adhered to a metal foil current collector with a binder, typically PVDF (polyvinylidene fluoride). Liquid electrolytes in lithium-ion batteries consist of lithium salts, such as $LiPF_6$ or $LiBF_4$ in an organic solvent, such as ethylene carbonate, dimethyl carbonate, and diethyl carbonate.

When a Li-ion cell is charged, the active positive electrode material is oxidized and the negative electrode is reduced. In other words lithium ions are de-intercalated from the positive electrode and intercalated into negative electrode through the electrolyte. The reverse occurs on discharge.

Organic solvents easily decompose on anodes during charging. However, when appropriate organic solvents are used as the electrolyte, the solvent decomposes on initial charging and forms a solid layer called the solid electrolyte interphase (SEI), which is electronically insulating yet provides sufficient ionic conductivity. The interphase prevents decomposition of the electrolyte after the second charge. Vast numbers of researches have been carried out to study the nature of this SEI formation.

Chapter 3

Nuclear Magnetic Resonance (NMR)

3.1 Introduction

In December 1945 Purcell, Torrey and Pound detected weak radiofrequency signals generated by atomic nuclei in 1 kg of paraffin wax. Similar independent experiments performed by Bloch, Hansen and Packard observed radiofrequency signals generated from nuclei in water[1]. These series of experiments were the birth of the famous field known as *Nuclear Magnetic Resonance* (NMR). In the years since then, NMR has become an invaluable physical tool for investigating matter in incredibly diverse areas.

NMR is a property that magnetic nuclei have in a magnetic field and applied electromagnetic (EM) pulse or pulses, which cause the nuclei to absorb energy from the EM pulse and radiate this energy back out. The energy radiated back out is at a specific resonance frequency which depends on the strength of the magnetic field and other factors. This allows the observation of specific quantum mechanical magnetic properties of atomic nuclei.

One can understand the science behind the NMR by classical physics or quantum physics. However for the sake of the simplicity, combination of both classical and quantum descriptions are used in the following section.

3.2 Nuclear Spins

Nuclei	Unpaired Spins (Protons/Neutrons)	Net Spin I	γ (MHz/T)
^{1}H	1/0	1/2	42.58
^{2}H	1/1	1	6.54
^{31}P	1/0	1/2	17.25
^{23}Na	1/2	3/2	11.27
^{14}N	1/1	1	3.08
^{13}C	0/1	1/2	10.71
^{19}F	1/0	1/2	40.08

Table 3.1: Gyromagnetic ratios of some commonly used isotopes[2].

Spin $\boldsymbol{I}$ is a fundamental characteristic of a nucleus. Some nuclei have integral spins and some others have half integral spins while yet other nuclei have no spin at all (Ex: ^{12}C, ^{16}O, ^{32}S). The combination of spin and charge generates a magnetic moment $\boldsymbol{\mu}$, which is proportional to the spin, govern by the Eqn. 3.2.1.

$$\boldsymbol{\mu} = \gamma \boldsymbol{I} \tag{3.2.1}$$

Where γ is gyromagnetic ratio, which is specific for every nucleus (Table 3.1).

3.3 Nuclear Zeeman Effect

Once a non-zero magnetic moment is placed in an external magnetic field (Zeeman Field) B, from classical physics equations the torque on the magnetic moment is given by,

$$\boldsymbol{\tau} = \boldsymbol{\mu} \times \boldsymbol{B} \tag{3.3.1}$$

Since $\boldsymbol{\tau} = \frac{d\boldsymbol{I}}{dt}$, with Eqn. 3.2.1, Eqn. 3.3.1 can be re-written as,

$$\frac{d\boldsymbol{\mu}}{dt} = \gamma \left(\boldsymbol{\mu} \times \boldsymbol{B} \right) \tag{3.3.2}$$

Assume the external magnetic field is directed in z-direction. i.e. $\boldsymbol{B}_0 = B_0 \boldsymbol{k}$. After substituting it in Eqn. 3.3.2 individual x, y and z components become,

$$\frac{d\mu_x}{dt} = \gamma\mu_y B_0 \tag{3.3.3}$$

$$\frac{d\mu_y}{dt} = -\gamma\mu_x B_0 \tag{3.3.4}$$

$$\frac{d\mu_z}{dt} = 0 \tag{3.3.5}$$

Solutions to these coupled equations are,

$$\mu_x(t) = \mu_x(0)\cos(\omega_0 t) \tag{3.3.6}$$

$$\mu_y(t) = -\mu_y(0)\sin(\omega_0 t) \tag{3.3.7}$$

$$\mu_z(t) = \mu_z(0) \tag{3.3.8}$$

Where $\omega_0 = \gamma B_0$. According to Eqn. 3.3.6, 3.3.7 and 3.3.8 the spins precess about the axis of the external magnetic field (z-axis in this case, Fig. 3.3.1).

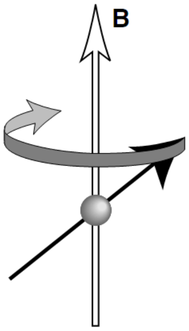

Figure 3.3.1: Nuclear precession about the external magnetic field.

This interaction is called *Nuclear Zeeman Interaction.* The frequency of the precession is called *Larmor frequency* and is proportional to the external magnetic field.

$$\omega_0 = \gamma B_0 \tag{3.3.9}$$

3.4 Nuclear Magnetization of an Ensemble of Spins

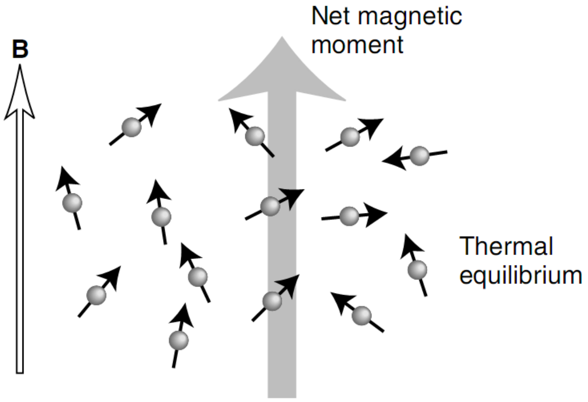

Figure 3.4.1: Net Magnetization at thermal equilibrium.

So far only one magnetic moment is considered in this description. However an NMR sample contains a large number of magnetic moments. If this kind of sample is placed in an external magnetic field in the z-direction, a nuclear magnetization $\boldsymbol{M}$, in the z-direction is established (Fig. 3.4.1) because of unequal population of two possible quantum states[1]. If N_1 and N_2 are the number of spins per unit volume in the respective states, the population ratio under thermal equilibrium is given by the *Boltzmann distribution*,

$$\left[\frac{N_2}{N_1}\right] = e^{-\frac{\hbar\omega_0}{k_B T}} \tag{3.4.1}$$

Summing over all $\boldsymbol{\mu}_i$ in the ensemble, the bulk magnetization $\boldsymbol{M}$ will be,

$$\boldsymbol{M} = \sum_i \boldsymbol{\mu}_i \tag{3.4.2}$$

Now the dynamics we discussed of a spin can be extend to an ensemble. The modified Eqn. 3.3.2 will be,

$$\frac{d\boldsymbol{M}}{dt} = \gamma\left(\boldsymbol{M} \times \boldsymbol{B}\right) \tag{3.4.3}$$

---

[1] Two quantum states of a proton in a magnetic field are spin-up and spin-down. Spin-up: protons with magnetic moments parallel to the external filed. Spin-down: protons with magnetic moments anti-parallel to the external field.

3.5 Interaction with an RF pulse

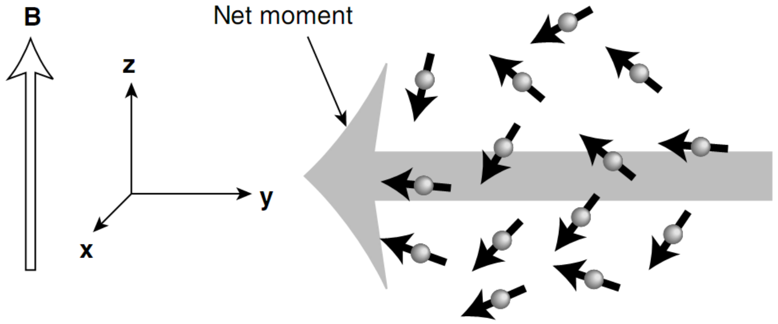

Figure 3.5.1: Spin distribution after a $\pi/2$ pulse.

All the equations, which have been discussed up to now were derived in the laboratory frame. Let's consider a rotating frame with an angular velocity ω_0. In such a frame the precessing magnetization can be treated as static. Now consider an RF (radio frequency) signal having a frequency of ω applied in the xy-plane of the system described by $\boldsymbol{B}_{RF} = B_{rf}\cos(\omega t)\boldsymbol{i} + B_{rf}\sin(\omega t)\boldsymbol{j}$. Then it can be shown that the effective magnetic field $\boldsymbol{B}_{eff}$ in the rotational frame will be,

$$\boldsymbol{B}_{eff} = B_{rf}\boldsymbol{i} + \left(B_0 - \frac{\omega}{\gamma}\right)\boldsymbol{k} \tag{3.5.1}$$

If the applied RF pulse is matched with the Lamor frequency, i.e $\omega = \omega_0$. the effective magnetic field can be considered as a static field introduced along the x-axis. The RF flips the magnetic moment off of the z-axis with an angle depending on the length of the pulse applied[2] (Fig. 3.5.1).

3.6 Spin-Lattice and Spin-Spin Relaxations

Suppose a $\pi/2$ pulse[3] is applied to the sample in its thermal equilibrium. The net equilibrium magnetization will flip to the xy-plane. The mechanism that nuclei relax back to their equilibrium (align parallel or anti-parallel to the external field $\boldsymbol{B}_0$) is called *Longitudinal relaxation* or *Spin-lattice relaxation* and the characteristic spin-lattice relaxation time is denoted by T_1. Only the z-component of the magnetization is affected by this phenomenon.

---

[2] The flip angle is proportional to the length of the pulse.

[3] RF pulse that flips the magnetization to the xy-plane from z-axis.

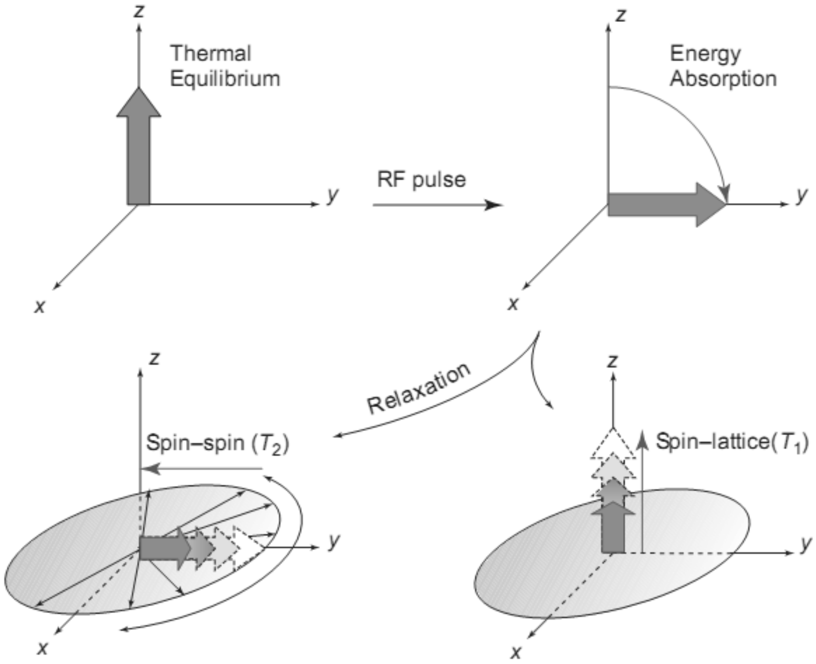

Figure 3.6.1: Spin relaxations.

Spin-spin relaxation governs the coherence of the spins in the xy-plane. Once the spins are perturbed by the RF pulse they all have the same phase. The precession speeds change over time due to slightly different environment that each spin feels. This reduces the transverse magnetization. Therefore this is called *Transverse relaxation* or *Spin-spin relaxation* and denoted by T_2. Including these T_1 and T_2 effects, the x, y and z components of the Eqn. 3.4.3 can be written as,

$$\frac{dM_x}{dt} = \gamma\left(\boldsymbol{M}\times\boldsymbol{B}\right)_x - \frac{M_x}{T_2} \tag{3.6.1}$$

$$\frac{dM_y}{dt} = \gamma\left(\boldsymbol{M}\times\boldsymbol{B}\right)_y - \frac{M_y}{T_2} \tag{3.6.2}$$

$$\frac{dM_z}{dt} = \gamma\left(\boldsymbol{M}\times\boldsymbol{B}\right)_z - \frac{M_z - M_0}{T_1} \tag{3.6.3}$$

Eqn. 3.6.1, 3.6.2 and 3.6.3 are known as *Bloch's equations.* Solutions for these equations are,

$$M_x(t) = M_x(0)\cos(\omega_0 t)e^{-\frac{t}{T_2}} \tag{3.6.4}$$

$$M_y(t) = -M_y(0)\sin(\omega_0 t)e^{-\frac{t}{T_2}} \tag{3.6.5}$$

$$M_z(t) = M_z(0)\left(1 - e^{-\frac{t}{T_1}}\right) \tag{3.6.6}$$

3.7 NMR Detection

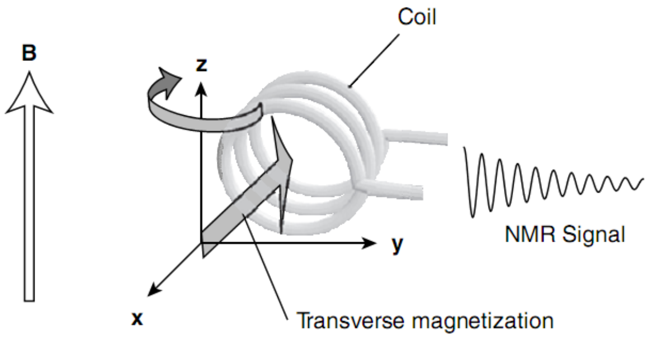

Figure 3.7.1: NMR signal detection.

After all of this occurs, the oscillating transverse magnetization is detected by the pick-up coil on the NMR probe and the corresponding electrical signal is sent to the NMR spectrometer and finally to the computer. This time scaled signal is called FID or *Free Induction Decay.* Fourier transformed FID gives us a frequency spectrum which contains information including chemical shifts, different interactions such as dipolar, quadrupolar coupling about the sample as shown in Fig. 3.7.2.

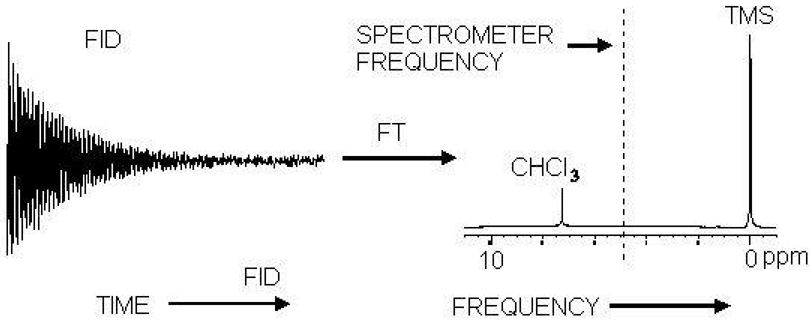

Figure 3.7.2: NMR FID and its Fourier transformed spectrum.

In any condensed phase, a nuclear spin experiences a great number of interactions. They can be categorized as external and internal interactions. External interactions, Zeeman and RF were already discussed in the previous section. Major internal spin interactions/Hamiltonians in solids will be discussed next.

3.8 Chemcial Shift

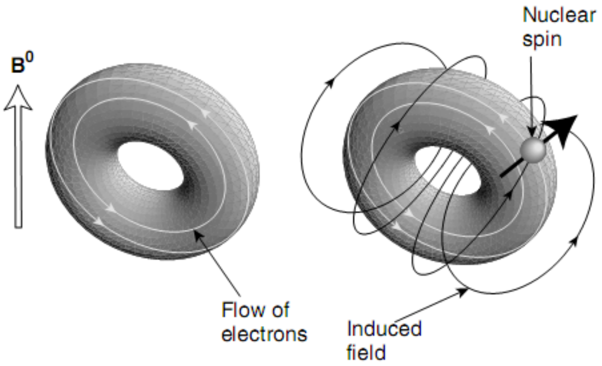

Figure 3.8.1: Mechanism of the Chemical Shift.

The signal frequency that is detected in NMR spectroscopy is proportional to the magnetic field applied to the nucleus. This would be a precisely determined frequency if the only magnetic field acting on the nucleus was the externally applied field. Nevertheless the response of the atomic electrons to that externally applied magnetic field is such that their motions produce a small magnetic field at the nucleus which usually acts in opposition to the externally applied field as illustrated in Fig. 3.8.1. The induced filed on Jth spin is,

$$\boldsymbol{B}_{ind,j} = \boldsymbol{\delta}_j B_0 \tag{3.8.1}$$

Here, δ_j represents a 3×3 matrix of real numbers called the *chemical shift tensor*. This change in the effective field on the nuclear spin causes the NMR signal frequency to shift. It is called a *chemical shift*. The magnitude of the shift depends upon the type of nucleus and the details of the electron motion in the nearby atoms and molecules. The precision of NMR spectroscopy allows this chemical shift to be measured, and the study of chemical shifts has produced a large store of information about the chemical bonds and the structure of molecules.

The full form of the chemical shift interaction of spin $\boldsymbol{I}_j$ can be written as,

$$\begin{aligned} \boldsymbol{H}_{CS,j} &= -\boldsymbol{\mu}_j.\boldsymbol{B}_{ind,j} \\ &= -\gamma_j \delta_{xz,j} B_0 \boldsymbol{I}_{x,j} - \gamma_j \delta_{yz,j} B_0 \boldsymbol{I}_{y,j} - \gamma_j \delta_{zz,j} B_0 \boldsymbol{I}_{z,j} \end{aligned} \tag{3.8.2}$$

In practice, chemical shifts are measured in parts per million (ppm or δ) relative to a reference resonance signal from a slandered molecule such as TMS (Tetramethylsilane).

$$\delta = \frac{\Omega - \Omega_{ref}}{\omega_0} \times 10^6 \tag{3.8.3}$$

Here, Ω and Ω_{ref} are the offset frequencies of the signal of interest and the reference signal respectively.

3.9 Dipole-Dipole Coupling

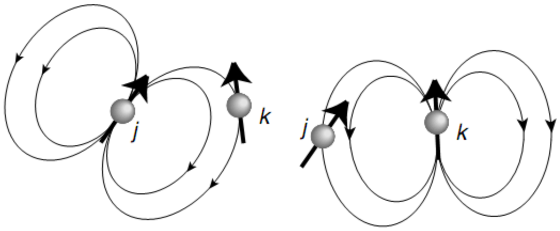

Figure 3.9.1: Magnetic loops generated by spin j (left) and spin k (right).

Since each nuclear spin is a magnet, the generated magnetic field loops around the surrounding space according to the direction of the spin magnetic moment (Fig. 3.9.1). A second nuclear spin may interact with the field and vice-versa. This mutual interaction is called *dipole-dipole coupling.*

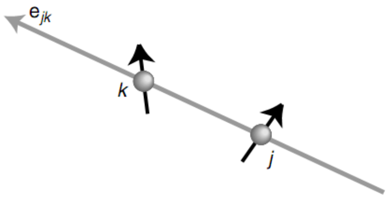

Figure 3.9.2: Unit vector parallel to the line joining the centers of the two spins.

The dipole-dipole coupling can be intermolecular or intramolecular. The full form the the dipole-dipole interaction Hamiltonian between spin $\boldsymbol{I}_j$ and $\boldsymbol{I}_k$ is resprestend as,

$$\boldsymbol{H}_{jk} = -\frac{\mu_0}{4\pi}\frac{\gamma_j\gamma_k}{r_{jk}^3}\left(3\left(\boldsymbol{I}_j.\boldsymbol{e}_{jk}\right)\left(\boldsymbol{I}_k.\boldsymbol{e}_{jk}\right) - \boldsymbol{I}_j.\boldsymbol{I}_k\right) \tag{3.9.1}$$

Where is a unit vector parallel to the line joining the centers of the two nuclei (Fig. 3.9.2). Dipole-dipole coupling is very useful in structural studies as it depends only on known physical constants and the inverse cube of the inter-nuclear distance.

3.10 Quadrupolar Coupling

Nuclei with a spin angular momentum quantum number greater than 1/2 are called *quadrupolar* nuclei because these nuclei possess, in addition to their magnetic dipole moment, an electric quadrupole moment.

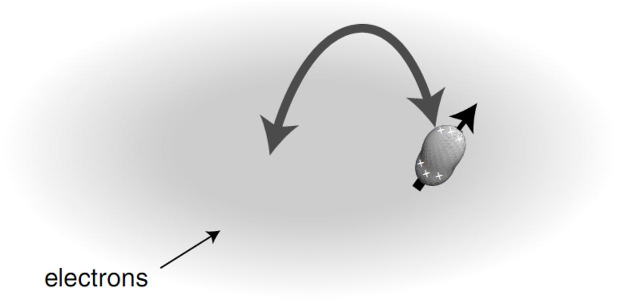

Figure 3.10.1: Surrounding electric gradient field.

Electric quadrupole moments may couple to its surrounding electric field gradient, which for a nucleus arises from asymmetric bonding environments. Quite often, this electric quadrupolar coupling is much stronger than the magnetic couplings to neighboring nuclei. The effect of such strong quadrupolar couplings on the NMR spectrum significantly decreases the NMR sensitivity and resolution. If the quadupolar interaction is much smaller than the Zeeman interaction, the secular quadrupolar interaction of spin $\boldsymbol{I}_j$ is given by,

$$\boldsymbol{H}_j \cong \omega_j \left(3\boldsymbol{I}_{jz}^2 - \boldsymbol{I}_j.\boldsymbol{I}_j\right) \tag{3.10.1}$$

Where ω_j is called the *quadruplar frequency* and for solids is given by,

$$\omega_j = \frac{3eQ_j}{4I_j\left(2I_j - 1\right)} V_{j,zz} \tag{3.10.2}$$

Here Q_j is the *electric quadrupole moment* of the nucleus, e is the charge of the proton and $V_{j,zz}$ is the component of the electric field gradient at the nucleus I_j.

3.11 MAS NMR

The main three NMR interactions in solids we have discussed, dipolar, chemical shift anisotropy and quadrupolar often lead to very broad and featureless spectra. MAS (*Magic Angle Spinning*) is a powerful technique that averages these interactions and makes broad lines narrow. The chemical shift anisotropy averages to a non-zero value.

The nuclear dipole-dipole interactions, between magnetic moments of nuclei average to zero only at a specific angle. Non-secular[4] parts of the Hamiltonian (Eqn. 3.9.1) can be discarded in high magnetic field and the remaining secular part can be divided into two parts depending on the two spins whether they are homo-nuclear or hetero-nuclear. Homo-nuclear part is given by,

$$\boldsymbol{H}_{homo} = d_{jk}\left(3I_{jz}I_{kz} - \boldsymbol{I}_j.\boldsymbol{I}_k\right) \tag{3.11.1}$$

and the hetero-nuclear part is,

$$\boldsymbol{H}_{hetero} = d_{jk}2I_{jz}I_{kz} \tag{3.11.2}$$

Here, d_{jk} is known as *secular dipole-dipole* coupling and given by,

$$d_{jk} = b_{jk}\frac{1}{2}\left(3\cos^2\Theta_{jk} - 1\right) \tag{3.11.3}$$

Θ_{jk} is the angle between e_{jk} and the external magnetic field e_z. The coupling constant b_{jk} depends on the distance between spins and the orientation. There is a solution to Eqn. 3.11.3 that makes d_{jk} zero and hence $\boldsymbol{H}_{homo}$ and $\boldsymbol{H}_{hetero}$ become zero.

$$3\cos^2\Theta_{jk} - 1 = 0 \tag{3.11.4}$$

That solution of Eqn. 3.11.3 is called the *Magic Angle*, that is 54.74^0 and a rapid spinning (1 - 70 KHz) of a sample at that angle during the NMR experiment is called MAS NMR or *Magic Angle*

---

[4] Terms that do not commute with Zeeman Hamiltonian.

Spinning Nuclear Magnetic Resonance (Fig. 3.11.1).

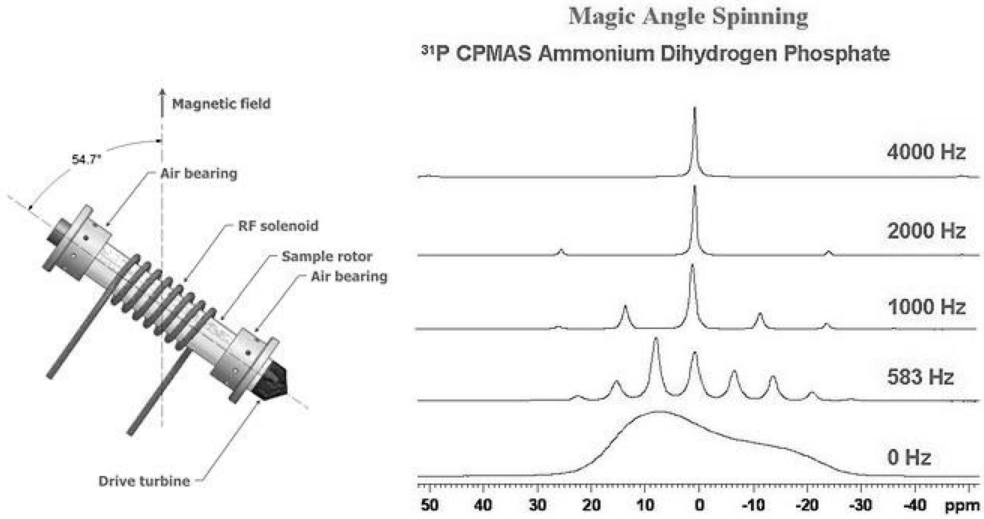

Figure 3.11.1: MAS spinning setup (left), MAS spectra (right).

In order to achieve high resolution, the angle must be set very precisely. This is commonly done by looking at the ^{79}Br signal of KBr. The intensity of the spinning sidebands for the satellite transition of ^{79}Br is strongly related to the precision of the magic angle. The sidebands appear as rotational echoes in the ^{79}Br FID. The more rotational echoes the stronger the sidebands and therefore the more precise the angle setting. Although any quadrupolar isotope with strong satellite transition sidebands can be used for this purpose, the ^{79}Br of KBr is particularly convenient as the resonance is very close to ^{13}C, has a short T$_1$, and can be seen easily in one scan.

3.12 Single Pulse Experiment

This is one of the simplest and most basic experiments in NMR. The pulse sequence used is called *single pulse sequence*. An RF pulse is applied to the sample. The magnetization flips off of the z-axis ($\boldsymbol{B}_0$ field direction). The proper pulse width and amplitude will knock the magnetization down to the xy-plane.

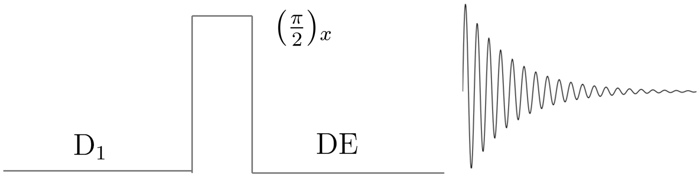

Figure 3.12.1: Single pulse sequence.

The interpulse delay (relaxation delay) D_1 serves to allow the spin system to relax back towards equilibrium. This is important for achieving the maximum signal-to-noise ratio. If the spin system doesn't relax sufficiently (called saturation) the relative intensity of the observed NMR peaks will suffer. The longer the relaxation delay, the closer the spin system gets to equilibrium. A long relaxation delay means a long experiment, therefore some type of compromise is made in practice. D_1 is generally about 5-10 times of the T_1 of a particular nuclear.

The dead time, DE, is a short delay between the end of the pulse and the beginning of acquisition. This is needed for the electronics of the system to stabilize following the high power RF pulse.

3.13 Spin Echo Experiment

The spin echo is one of the most fundamental building blocks for NMR pulse sequences. Its main purpose is to refocus the magnetization.

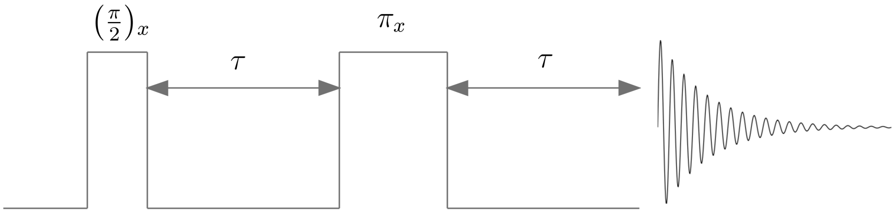

Figure 3.13.1: Spin-Echo pulse sequence.

A $(\pi/2)_x$ pulse is first given to create magnetization along the $-y$ axis of the rotating frame. During the first delay period τ, the magnetization rotates in the xy plane at a rate of Ω. The $(\pi)_x$ pulse rotates the magnetization 180 degrees about the x axis. During the second delay period, the magnetization again rotates in the xy plane at a rate Ω, in the same direction as during the first delay. At the end of the second delay, the magnetization is on the y axis and the acquisition of the FID is started.

3.14 Inversion Recovery Experiment

This pulse sequence is used to measure the spin-lattice relaxation time, T_1. After the spin system is prepared at equilibrium (during the recycle delay time), the spin magnetization is inverted into the $-z$ direction through application of a π pulse as shown in Fig. 3.14.1.

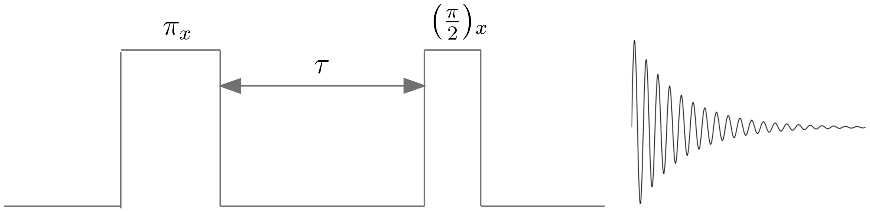

Figure 3.14.1: Inversion recovery pulse sequence.

During the evolution time τ, the inverted magnetization recovers along the $+z$-axis towards its equilibrium value of $\boldsymbol{M}$. The goal is to monitor the recovered magnetization as a function of τ. In order to detect the recovering magnetization, a $\pi/2$ along the x-axis is applied. At this point, the free induction decay is recorded. The magnetization as a function of τ is given by Eqn. 3.14.1 and is illustrated in Fig. 3.14.2. T_1 can be extracted from the recovery profile.

$$M_z(\tau) = M_0\left(1 - 2e^{-\frac{\tau}{T_1}}\right) \tag{3.14.1}$$

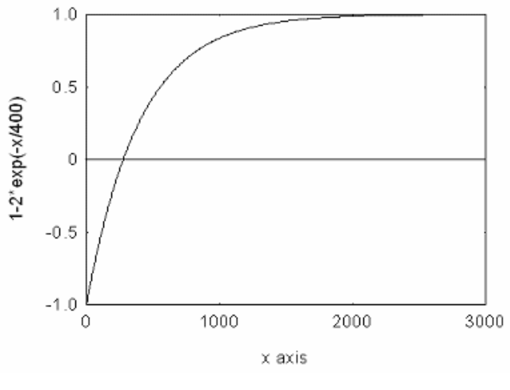

Figure 3.14.2: T_1 profile (M vs. τ).

3.15 Saturation Recovery Experiment

Another way to measure spin-lattice relaxation is to prepare the spin system in a saturated state and monitor its free evolution towards equilibrium. This approach has an advantage over inversion recovery in that it takes much less time to initially prepare the spins, provided the system can be saturated. Saturation recovery is the preferred method for the study of long T_1 (T_1>10s) spins.

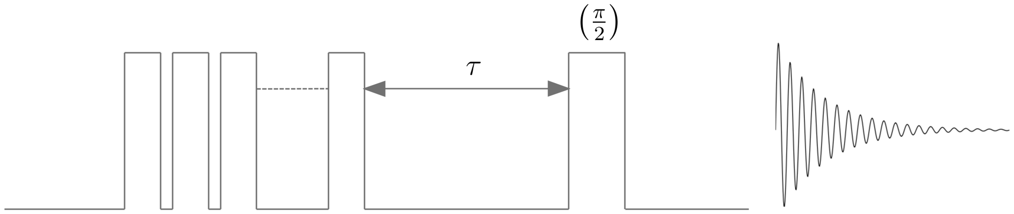

Figure 3.15.1: Saturation recovery pulse sequence.

The saturated condition is achieved by subjecting the spin system to a rapid succession of saturation pulses. This pulse-train is typically comprised of 10 to 100 high-power $\pi/2$ or lower pulses separated by a delay greater than or on the order of T_2. After the spins are prepared in a saturated state, an evolution time τ is allowed for the spin system to evolve towards its equilibrium value. As with the inversion recovery sequence, the goal is to monitor the recovered magnetization as a function of τ. The recovering magnetization is detected via application of a $\pi/2$ pulse. The magnetization as a function of τ is given by Eqn. 3.15.1 and is illustrated in Fig. 3.15.2. T_1 can be extracted from the recovery profile.

$$M_z(\tau) = M_0\left(1 - e^{-\frac{\tau}{T_1}}\right) \tag{3.15.1}$$

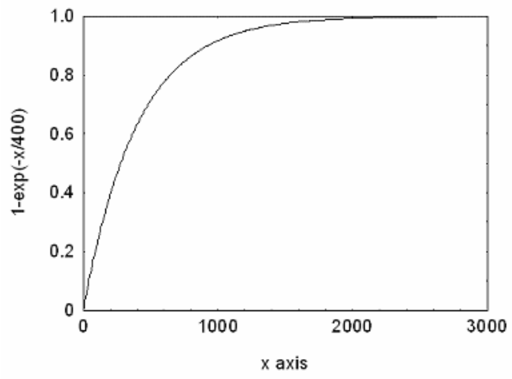

Figure 3.15.2: T_1 profile (M vs. τ).

Chapter 4

Electrochemically Discharged CF$_x$

4.1 Introduction

The lithium/carbon monofluoride cathode system is known to have the highest theoretical energy density among solid cathode systems. Li/CF$_x$ batteries[5] have remained attractive because of their very high energy density, long storage life, very good safety record, wide temperature range and very low self-discharge. However its use is restricted to specialized applications where superior performance is required such as aerospace, military and medical applications due to the relatively high cost of CF$_x$.

Typically x is approximately equal to 1 for commercial grade Li/CF$_x$ battery material. The electrolyte typically consists of lithium tetrafluoroborate (LiBF$_4$) in gamma-butyrolactone or lithium hexafluoroasenate (LiAsF$_6$) in a mixture of propylene carbonate (PC) and dimethoxyethane (DME)[6]. The chemical reaction of the discharging process is summarized below.

$$\begin{aligned} nLi &\rightarrow nLi^{+} + ne^{-}(\text{anode reaction}) \\ ne^{-} + (CF_x)_n &\rightarrow nC + nF^{-}(\text{cathode reaction}) \\ nLi + (CF_x)_n &\rightarrow nLiF + nC\ (\text{overall reaction}) \end{aligned}$$

The CF$_x$ is converted into elemental carbon which is more conductive than CF$_x$ thereby lowering the internal impedance, improving the voltage regulation and the efficiency. At the same time LiF is formed and precipitates out of the structure during the course of discharge.

Electrochemical studies have shown significant differences between each type of CF_x: prepared from carbon with a fiber morphology, hereafter referred to CF_x – F or F-type; prepared from petroleum coke, hereafter referred to as CF_x – C or C-type; and prepared from graphite, hereafter referred to as CF_x – G, or G-type. Although the fundamentals of the electrochemical discharging process are known, the structure of the CF_x cathode during the discharge and the mechanism of the defluorination process at the molecular level that might be responsible for the electrochemical differences are not known. This study is focused on NMR investigations of these three different types of CF_x materials to determine their structural/chemical differences, discharge mechanism and possible intermediate compound formation during discharge.

4.2 Experimental

CF_x materials (F, C and G types) were prepared by fluorination of fibrous, amorphous coke and standard graphite respectively at 300–600 ^{0}C provided by commercial sources. Unfortunately no further details were provided by the vendor. CF_x cathode mixes were prepared with raw CF_x, conductive carbon, and binder materials.

Li/CF_x experimental cells were constructed with the three types of CF_x and they were discharged to various depth of discharge (DoD) under a 6 month discharge rate at 37 ^{0}C.

^{13}C (spin 1/2) MAS NMR, is widely used, despite its relative paucity in naturally occurring carbon (approximately 1%). Because of low natural abundance and generally long spin–lattice relaxation time (T_1), spectrum acquisition on samples which have not been experimentally enriched in ^{13}C takes a long time. A Varian Inova 500 MHz spectrometer and Doty low C/F background probe were used to perform ^{13}C MAS NMR measurements. Samples were packed in 4 mm rotors and spun up to 12–14 kHz. Tetramethylsilane (TMS) was used as the external reference.

^{19}F (spin 1/2) MAS NMR, is relatively commonly measured, yields strong signals and has a wide chemical shift range. ^{19}F MAS NMR measurements were conducted with a 300 MHz Varian S Direct Digital Drive NMR spectrometer (the 300 MHz spectrometer was used because of the availability of higher spinning speeds) at spinning speeds from 32 kHz to 37 kHz in 1.6 mm rotors. A 90_x- 180_y pulse echo sequence was used to minimize the probe background signal. An aqueous solution of lithium trifluoromethylsulfonate was used as an external reference for fluorine at -77.8

ppm relative to the common reference $CFCl_3$. All the spectral analysis and deconvolution are performed by MestReNova software. Other physical characterizations were provided by Dr. Hong Gan at *Greatbatch, Inc.*

4.2.1 Deconvolution calibrations

The accuracy of deconvolution techniques and associated software was tested with known physical mixtures of raw CF_x – G and LiF. Four different mixtures of LiF/CF_x – G (LiF by weight – 10%, 20%, 50%, 75%) were investigated.

4.2.2 Slow (Greatbatch) discharged cells

CF_x- F (%)	CF_x- C (%)	CF_x- G (%)
1.2	1.2	1.2
7.5	7.9	7.8
22.2	23.0	23.3
45.2	46.5	45.4
67.2	69.8	67.9
89.3	92.1	86.7
97.0	99.4	95.6

Table 4.1: DoD levels of Greatbatch discharged samples.

Li/CF_x cells were electrochemically discharged for 6 months. The cell discharge voltage profiles and cell internal resistance vs. the DoD were obtained. Cathode materials were extracted at different DoD levels (Table 4.1) and washed thoroughly with DME to remove residual electrolyte salt.

^{19}F and ^{13}C were conducted (1–3 months) after sample preparation. Apart from MAS NMR measurements, nine samples (three of each type) were picked among 21 samples to perform ^{7}Li and ^{19}F T_1 measurements with inversion recovery pulse sequence.

4.2.3 Fast (Hunter) discharged cells

A focus of this study was to detect and investigate any shortlived intermediate species during the discharge process. NMR measurements were done in a short period of time (1–2 h) after cell discharge to improve the probability of detecting any metastable compounds. Six Li/CF_x batteries (two of each type) were electrochemically discharged at the Hunter lab with an Arbin battery cycler with a particular discharge protocol described below.

CF_x battery type	discharged time (h)	Target % DoD
F/C/G	309.12	46
F/C/G	537.60	80

Table 4.2: Battery discharge protocol at Hunter.

Cells were discharged at room temperature under 2.93 mA constant current according to Table 4.2. After the long discharge, cells were equilibrated at open circuit and discharged again for a short period of time (1 min) at higher rate (75 mA) just before cell disassembly and NMR experiments. One particular cell (type C) with an estimated DoD of 80% could not sustain the short discharge at 75 mA, due to the cell having exceeded the voltage limit set for the procedure. A possible reason for this is mentioned later. Therefore it was discharged for 3 min at 25 mA instead of 1 min at 75 mA to acquire the target DoD.

Each battery was dissembled inside the argon filled glove-box. The cathode was extracted carefully and half of it was left alone and labeled as un-washed while the other half was rinsed with DME three times for 15 min each (labeled as washed). ^{13}C and ^{19}F MAS NMR studies of un-washed samples were performed immediately after the disassembly. Washed samples were left inside of the glove box antechamber for several hours to dry completely before NMR studies.

4.3 Results and Discussion

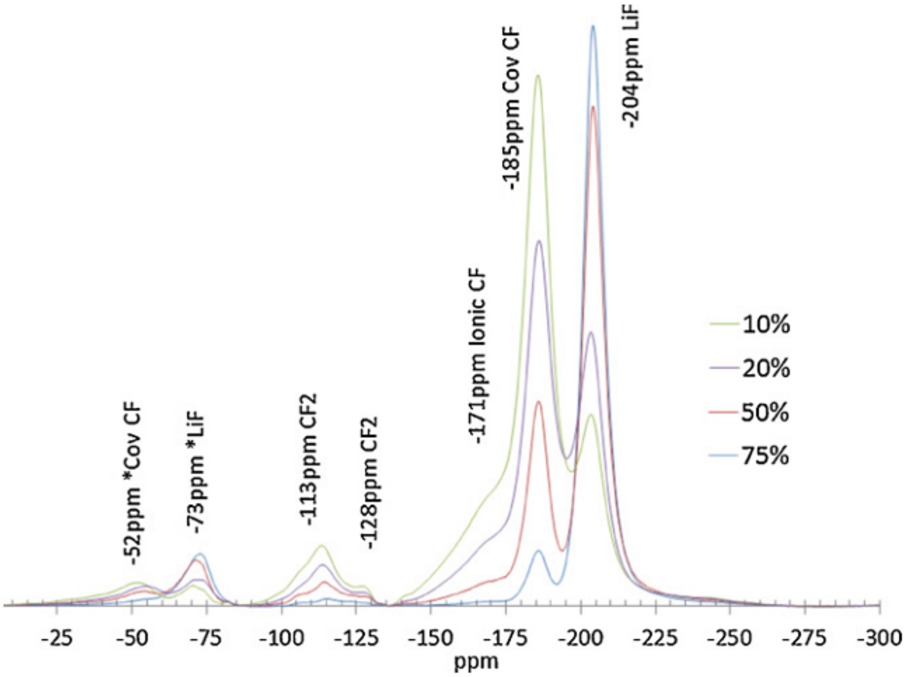

Figure 4.3.1: ^{19}F MAS NMR of manually mixed LiF/CF$_x$ mixtures. The percentages given above refer to the fraction of LiF in the mixture. Asterisks denote spinning sidebands.

High speed MAS at 32–37 kHz greatly reduces the homonuclear dipolar coupling broadening of ^{19}F spectra, shown in Fig. 4.3.1 for the case of mixtures of CF$_x$ and LiF. Sidebands were clearly identifiable and most of the features were easily distinguishable with no significant overlap. In discharged materials, four main features are prominent to different degrees depending on the sample that was studied. The most intense peak in all series at low discharge levels is around -184 to -187 ppm and was clearly larger for correspondingly lower level discharged samples, lower for higher level discharged samples, and assigned to covalent CF groups [7]. A semiionic CF peak is found around -170 ppm[6]. The broad peak around -113 to -116 ppm was assigned to CF$_2$ groups located at the edge of graphite layers [8, 7]. A relatively sharp Teflon^{TM} (present as a binder) peak occurs around -121 ppm. Upon discharging, the LiF resonance appears around -204 ppm[6]. Very slight changes of the positions of sidebands correspond to slight spinning speed variations. However this had a negligible effect on deconvolution and interpretation of the data.

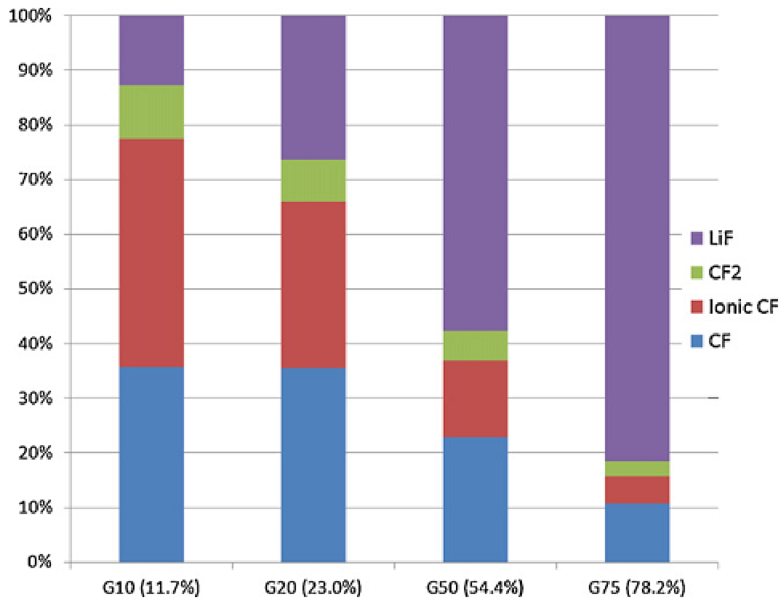

Figure 4.3.2: ^{19}F MAS NMR deconvolution of manually mixed LiF/CF_x mixtures. Numbers are molar percentages which correspond to weight percentage values in Table 4.3.

4.3.1 Deconvolution calibrations

Percent from known mixture	Percent from NMR deconvolution
10.0	10.3
20.0	22.1
50.0	51.4
75.0	77.2

Table 4.3: Comparison of weight percentage of LiF in known mixtures of CF_x – G and LiF with spectroscopic determination.

Right sidebands are not shown in the spectra (Fig. 4.3.1) for the sake of clarity but they have been included in the deconvolution shown in Fig. 4.3.2. LiF weight percentages were calculated from deconvolutions. Table 4.3 reveals that NMR measurements/deconvolution were very consistent with molar-weight-calculated values, although there is some uncertainty in deconvoluting the ionic and covalent CF features due to overlap (their ratios should not change in these spectroscopic standards).

4.3.2 Slow (Greatbatch) discharged batteries

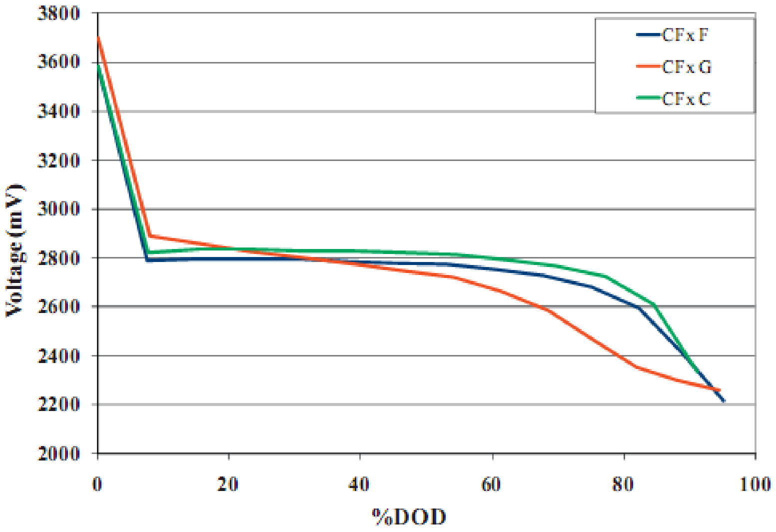

Figure 4.3.3: Discharge voltage profiles of CF_xF, CF_x G and CF_x C cells under 6 month discharge rate. Data provided by *Greatbatch, Inc.*

CF_x experimental cells were discharged under a six-month rate at 37 ^{0}C. The cell discharge voltage profiles are shown in Fig. 4.3.3. CF_x G cells show a more sloped discharge voltage profile than CF_x C and CF_x F cells. At beginning of life, CF_x G cells exhibit higher cell voltages than that of CF_x C and CF_x F cells. The CF_x G cell voltages gradually decrease and cross over at around 20% to 35% DoD resulting in lower cell voltages than that of CF_x C and CF_x F cells at later DoDs. The voltage profile of CF_x C cells is slightly higher than that of CF_x F cells throughout discharge. Both CF_x C and CF_x F cells exhibit a voltage plateau at around 2.8 V until ~60% DoD and then gradually decrease. The discharge voltages from all three types of CF_x cells merge to 2.3 V at approximately 95% DoD.

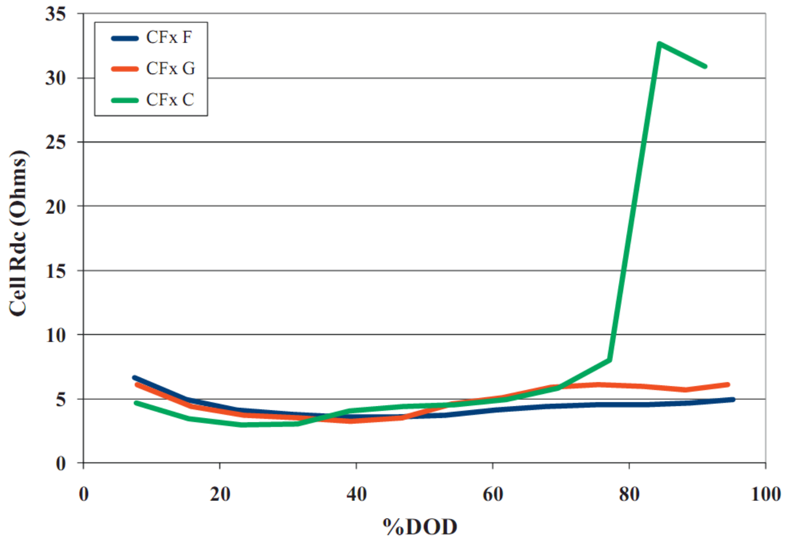

Figure 4.3.4: CF$_x$ type effect on cell internal Rdc change vs. %DoD. Data provided by *Greatbatch, Inc.*

Fig. 4.3.4 shows the relationship of the cell internal resistance (Rdc) vs. DoD. As expected, all cells exhibits decreased Rdc when they were discharged from BOL to $\sim$ 30% DoD due to the formation of carbon as one of the products. However, in the 2nd half of cell discharge, the cell Rdc starts to increase. For CF$_x$ C, the cells have the lowest Rdc from BOL to $\sim$ 35% DoD. Beyond 35% DoD, CF$_x$ C cells develop higher internal resistance relative to the cells from CF$_x$ G and CF$_x$ F. Beyond 80% DoD, CF$_x$ C cells exhibit a significant Rdc increase, about 7 times that of the other two CF$_x$ types. This could be related to the cell's response to the 75 mA pulse discharge described in the experimental section. Among the three types of CF$_x$, CF$_x$ F cells exhibits the best stability with the least Rdc increase throughout discharge.

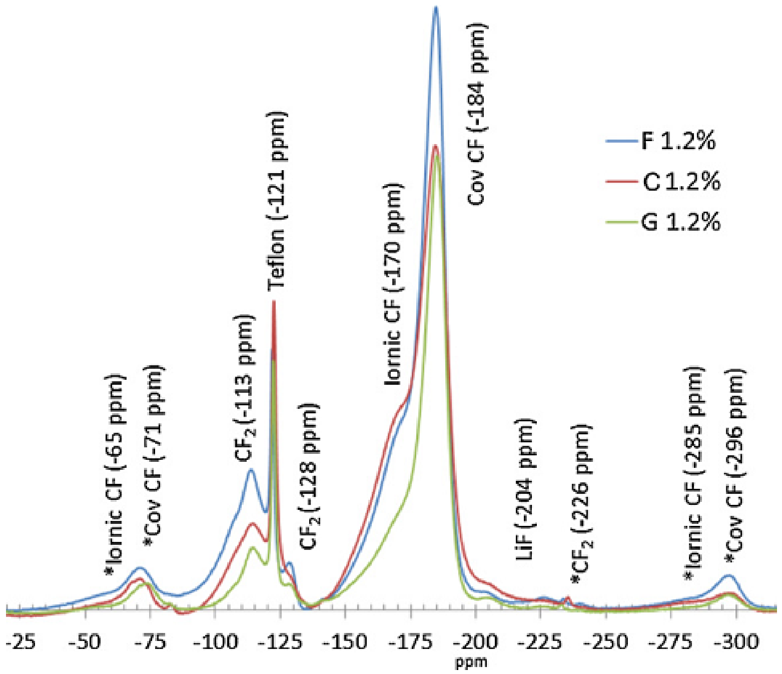

Figure 4.3.5: ^{19}F MAS NMR spectra of Greatbatch discharged nearly starting materials (F, C, G). Asterisks denote spinning sidebands.

^{19}F NMR spectra for very slightly discharged materials (1.2% DoD) are shown in Fig. 4.3.5. The G type has the maximum covalent CF content and lower semi-ionic CF. The sum of both covalent CF and semi-ionic CF in the 1.2% discharged F, C and G samples is about 81%, 84% and 89% respectively of the total fluorine. The spectral intensity of the Teflon^{TM} peak was excluded from the deconvolutions based on the assumption that it is chemically inert throughout discharge. As expected CF and LiF peaks dominate the lower DoD levels and higher DoD levels, respectively, as shown in Fig. 4.3.6 for the F series. G series shows the highest covalent CF throughout the whole range of discharge followed by C and F as shown in the deconvolutions displayed in Fig. 4.3.7. A structural re-arrangement could be responsible for the small increase of covalent CF in first few DoD levels (around 7 to 8%), although this value is close to the deconvolution uncertainty of these two species as described earlier in the context of the manually mixed standards. The CF content appears to decrease gradually upon discharging. In all three series, the semi-ionic CF is consumed faster than covalent CF in the electrochemically discharged cells, contrary to what was reported in chemically lithiated materials[6] (which is a comparatively very rapid process). Also no CF_3 groups around -50 to -70 ppm were noted as observed in previous results[6] for chemically lithiated CF_x.

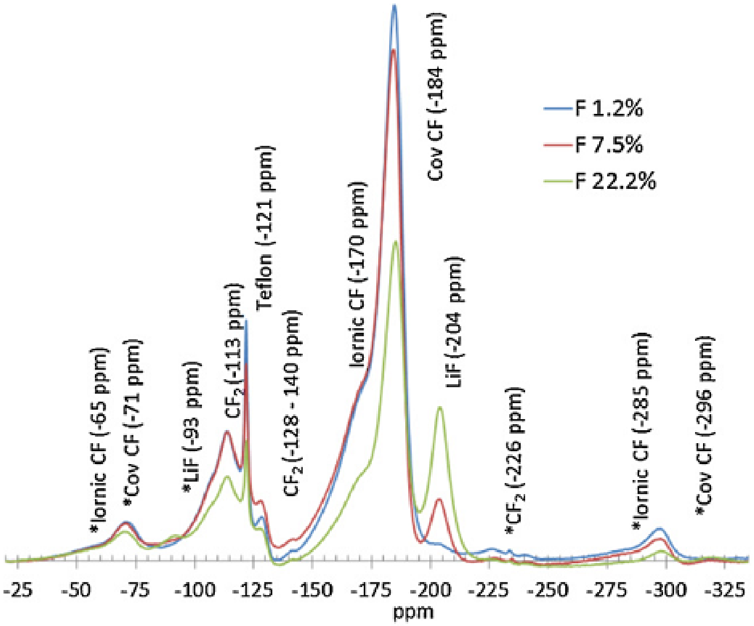

(a) Lower DoDs

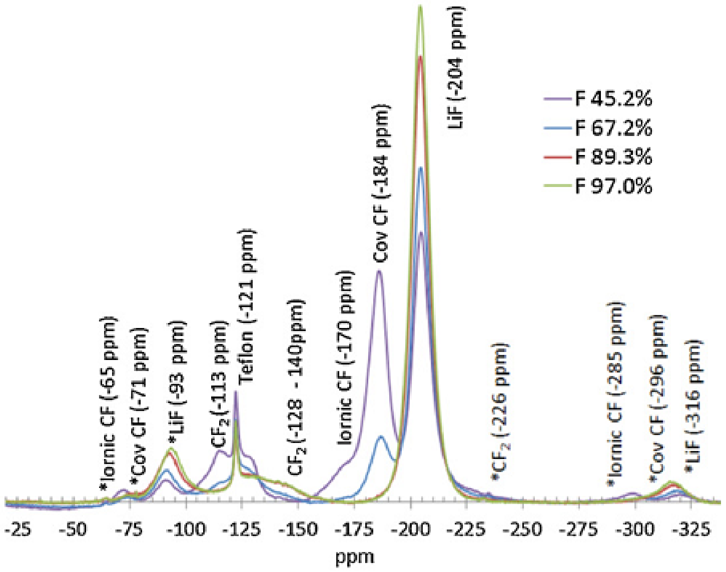

(b) Higher DoDs

Figure 4.3.6: ^{19}F MAS NMR spectra of Greatbatch discharged F Series. Asterisks denote spinning sidebands.

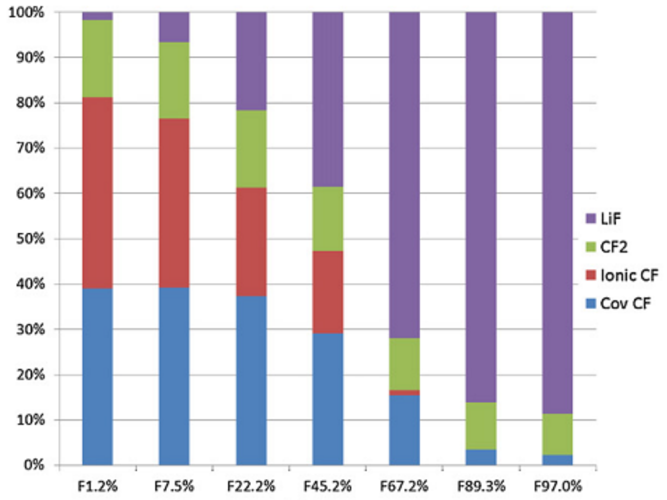

(a) F series

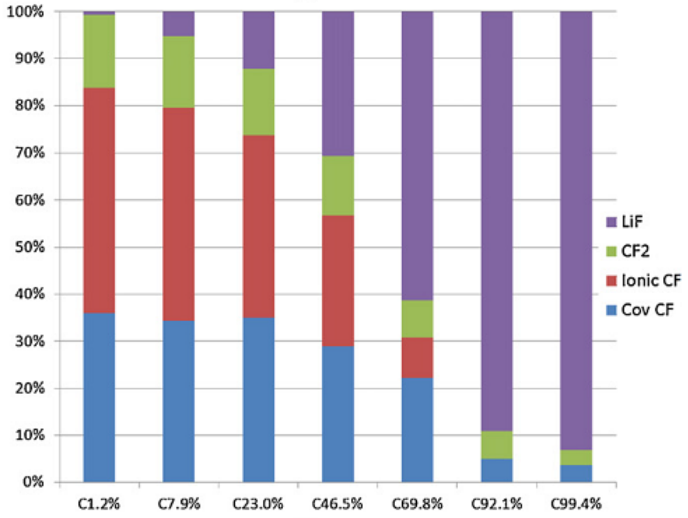

(b) C series

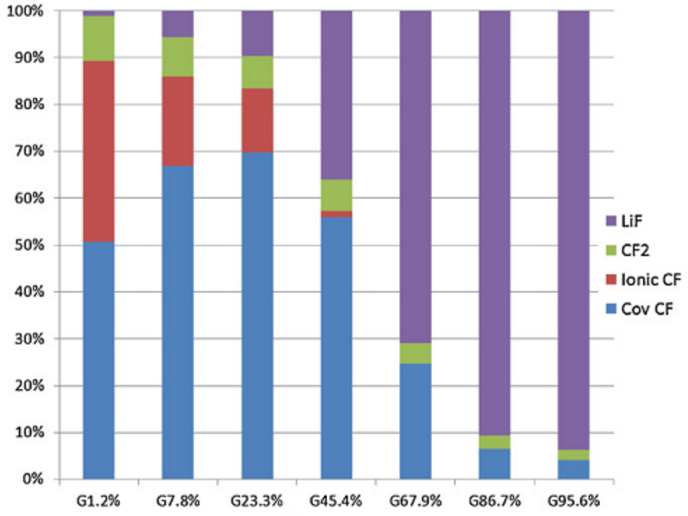

(c) G series

Figure 4.3.7: ^{19}F MAS NMR deconvolution of Greatbatch discharged F, C and G series.

^{13}C MAS NMR spectra were broader with lower SNR (signal to noise ratio) than ^{19}F MAS NMR spectra although each sample was run for at least 48 h. ^{13}C MAS NMR via cross-polarization by fluorine would help to reduce the relaxation time considerably. However cross-polarization data are not accurately quantifiable as the resonances are excited unequally. This is especially the case as the structural fluorine is reduced by lithiation. Two clear peaks were prominent despite the low SNR. The one around 82 to 90 ppm is assigned to CF[9] as shown in Fig. 4.3.8. The graphitic carbon is present around 125 ppm[10] while CF_2 and Teflon^{TM} peaks are overlapped heavily with the broad graphite carbon peak. As in the case of the ^{19}F results, the intensity of the Teflon^{TM} peak is not included in the ^{13}C deconvolutions which are displayed in Fig. 4.3.9.

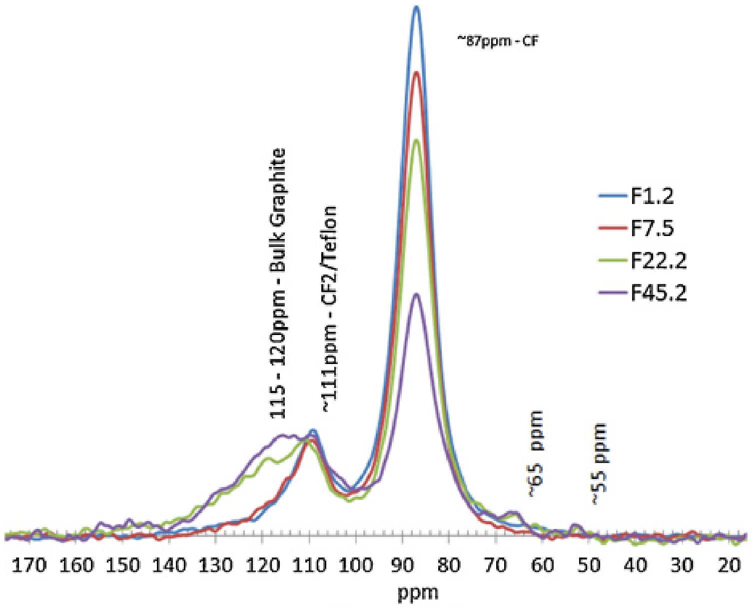

(a) Lower DoDs

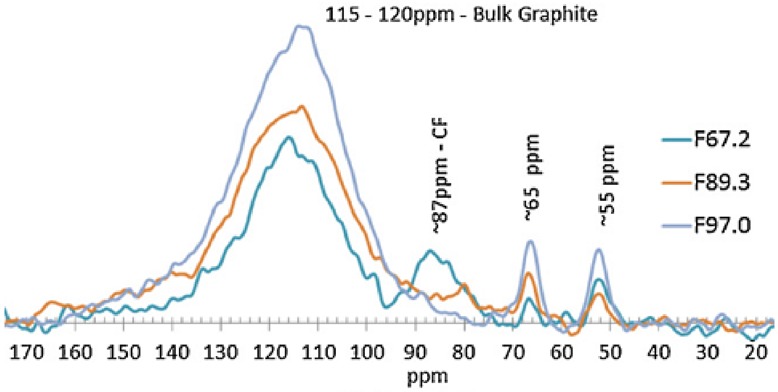

(b) Higher DoDs

Figure 4.3.8: ^{13}C MAS NMR spectra of Greatbatch discharged F series.

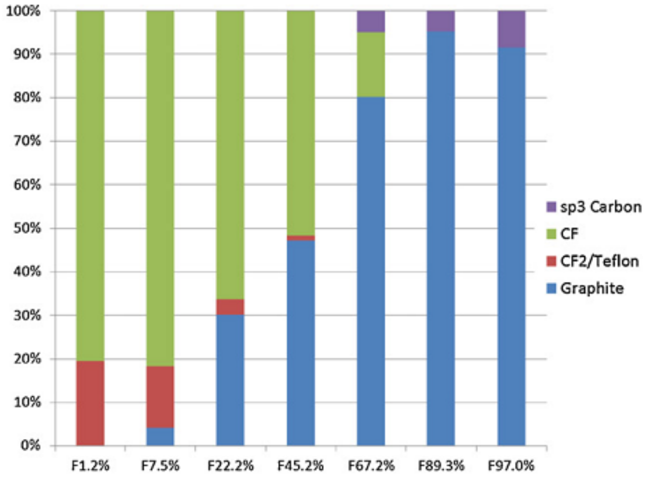

(a) F series

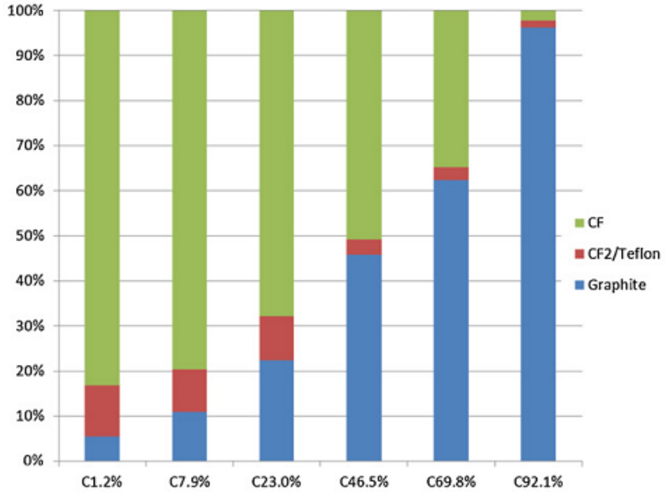

(b) C series

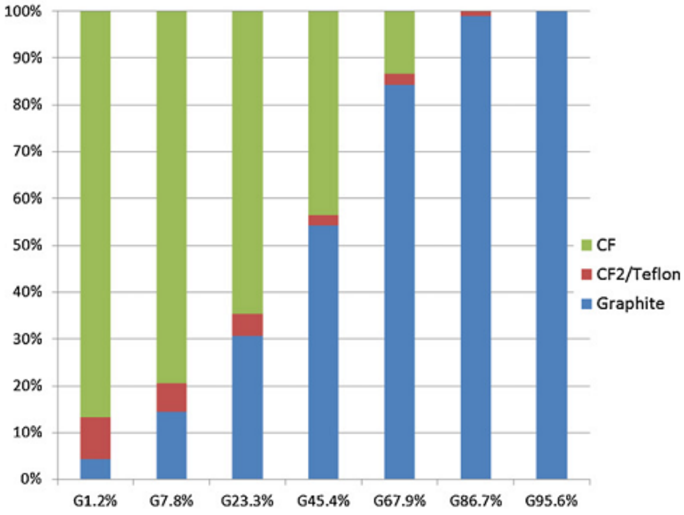

(c) G series

Figure 4.3.9: ^{13}C MAS NMR deconvolution of Greatbatch discharged F, C and G Series. The spectral results of C at 99.4% DoD are not included due to the low SNR characteristics of that sample. Although CF intensity appears in the ^{19}F spectra for the ~89% DoD samples, it does not show up distinctly in the ^{13}C deconvolutions due to large overlap.

In the ^{13}C MAS NMR spectra the CF peak resonates at 84–88 ppm. The ^{13}C NMR chemical shift of a carbon in a semi-ionic/ionic interaction with fluorine is near 89 ppm. Therefore this peak is not distinguishable from the covalent resonance. There are three closely spaced main features around −125 to −108 ppm assigned to bulk graphite, Teflon^{TM} and components that are generally attributed to CF_2 groups on the edge of the graphite planes. However, unlike the CF_2 edge groups seen in the ^{19}F MAS NMR data, this resonance disappears upon complete discharge. A complication, however, is the overlap of the broad graphite resonance, which of course becomes a severe problem for deconvolution at successively higher DoD. It is therefore concluded that if this is indeed representative of CF_2 groups, they are bound differently to the bulk CF, and are more accessible (e.g. surface vs. bulk sites) to the lithium than those seen in the fluorine data. However it is noted that even the ^{19}F data show decreasing CF_2 content with increasing DoD.

An sp^3 bonded carbon species around 55 ppm and another around 65 ppm, also assigned to sp^3 bonded carbon, appears in the middle stage of the electrochemically discharge samples.

The F series shows the maximum sp^3 bonded carbon amount which increases steadily from the middle to the end of discharge. The increase in bulk graphite content with increased discharge is also a consistent trend. Overall, the C series has the lowest CF consumption for a given nominal DoD while F and G maintain comparable amounts.

In order to check for possible differences in LiF formation between CF_x types, spin–lattice relaxation (T_1) measurements were performed. LiF is the only compound that appears in the ^{7}Li spectra as shown in Fig. 4.3.10. There is a clear increase of T_1 in all the series with increasing DoD. ^{7}Li T_1 of C and G series increase more slowly in comparison to the F series as shown in Fig. 4.3.11. One possible interpretation is that LiF precipitates out of the C/CF_x structure of the F series more readily as it more rapidly approaches bulk-like characteristics (i.e. longer T_1). Similar behavior of increasing T_1 with increasing DoD was observed in the ^{19}F measurements as shown in Fig. 4.3.12. Finely dispersed nanoscopic LiF that is formed in the early stages of discharge is generally characterized by shorter T_1 values compared to its bulk macroscopic phase due to structural defects. The more rapid exclusion of LiF may be an explanation of the superior performance of the F series material, since LiF is an insulator. For completeness, a ^{7}Li NMR spectrum of a nearly completely discharged sample is displayed in Fig. 4.3.10, and the spectrum is identical in appearance to that of bulk LiF.

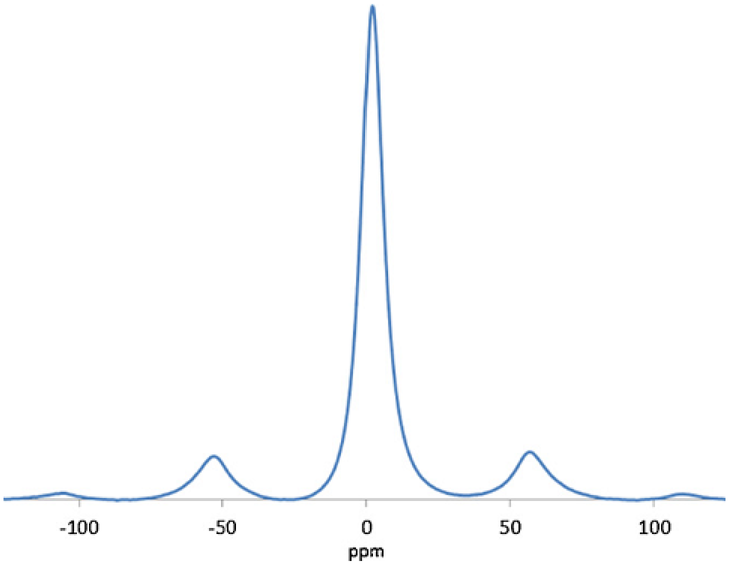

Figure 4.3.10: ^{7}Li MAS NMR spectrum of Greatbatch 99.4% discharged F sample.

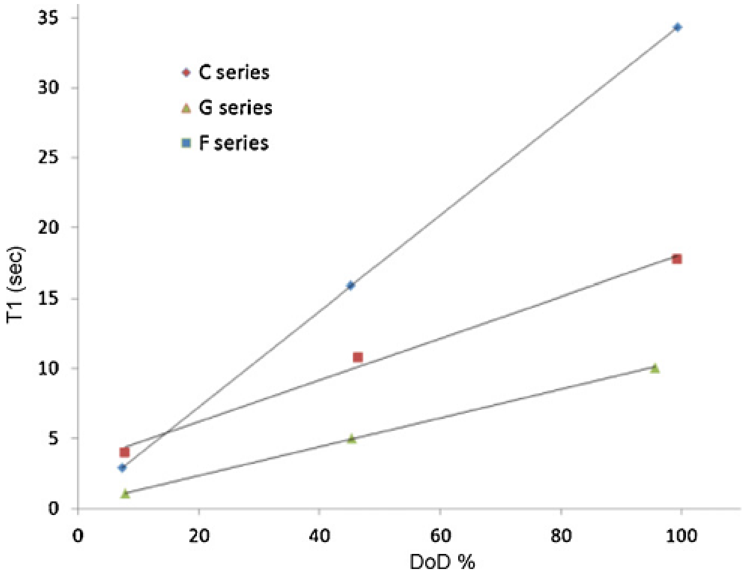

Figure 4.3.11: ^{7}Li MAS NMR T_1 measurements of Greatbatch discharged batteries. The straight lines are guides to the eye.

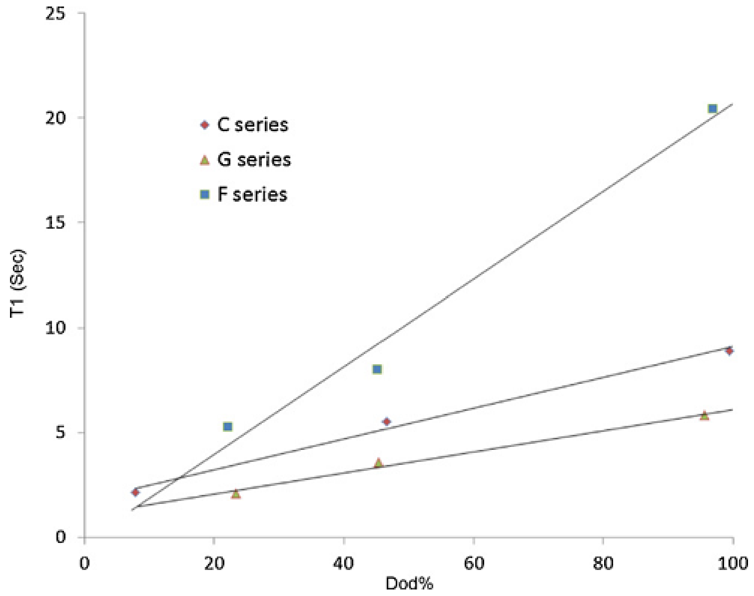

Figure 4.3.12: ^{19}F MAS NMR T_1 measurements of Greatbatch discharged batteries. The straight lines are guides to the eye.

4.3.3 Hunter discharged batteries

All the samples were run under comparable conditions described for the previous set. Although washed samples were rinsed with DME, a significant amount of $LiAsF_6$ was present in the samples as indicated by the feature at -69.5 ppm overlapped with left sidebands of LiF (slightly overlapped) and covalent CF (heavily overlapped) as shown in Fig. 4.3.13. Some samples were run at slightly lower spinning speed (32 kHz) due to mechanical issues and hence slight differences in the positions of sidebands are observed in the spectra. One clear observation is the LiF contents of Hunter discharged batteries are higher than those of Greatbatch discharged batteries especially in F and G series. That is, the actual LiF content is higher than the amount prescribed by the nominal DoD value. The reason for this could be the inhomogeneity of the sample in the different parts of the cathode which experienced different discharge rates. The ^{19}F deconvolutions are displayed in Fig. 4.3.14. It appears that all of the semi-ionic CF is consumed at the higher DoDs which is consistent with the results for the slower discharged samples.

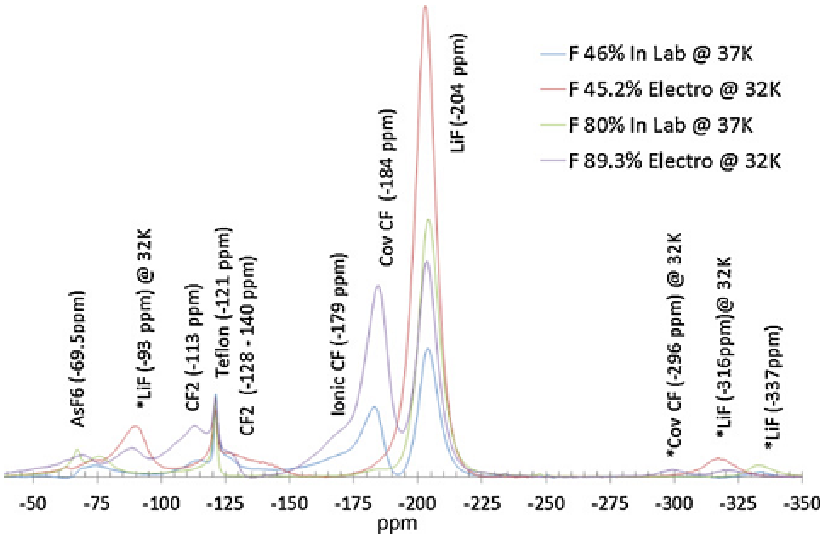

Figure 4.3.13: ^{19}F MAS NMR spectra of Hunter and Greatbatch discharged batteries. Asterisks denote spinning sidebands.

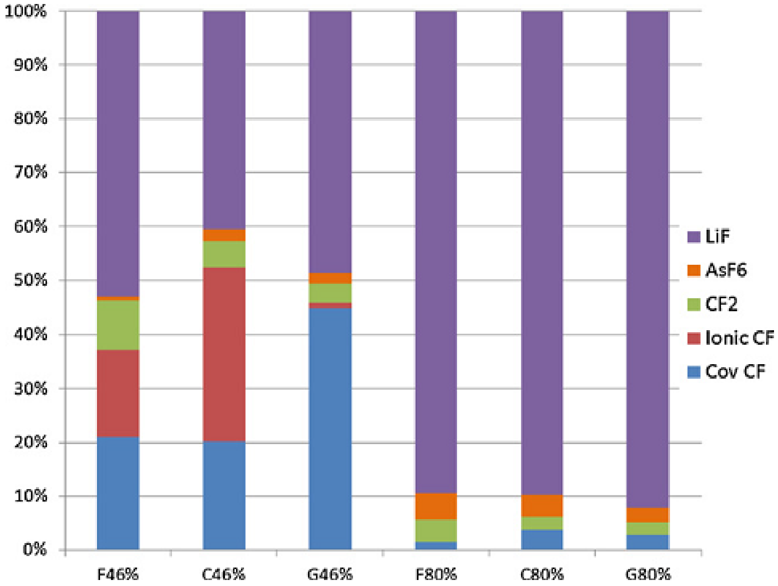

Figure 4.3.14: ^{19}F NMR deconvolution of Hunter discharged batteries for F, C and G series.

^{13}C NMR spectra reveal more subtle but important details. Three representative sets of spectra are displayed in Figs. 4.3.15 – 4.3.17, for washed and unwashed samples. The unwashed samples are characterized by large residual solvent peaks, despite the post-rinse vacuum treatment. The spectral intensity ratios of the two main peaks, graphite and CF, are similar in the washed and unwashed samples. Only F series consistently shows both features assigned to sp^3 bonded carbon at 55 and 65–68 ppm as in Greatbatch slow discharged samples. C series shows two sp 3 bonded carbon peaks in the same region. However at 80% DoD the peak around 65–68 ppm was absent. Also the peak around 55 ppm is not as strong as it is in the 46% DoD sample. The G Series is quite different. At 46%, no peaks are observed around 55 and 65–68 ppm. However a small peak around 65 ppm is observed at 80% DoD.

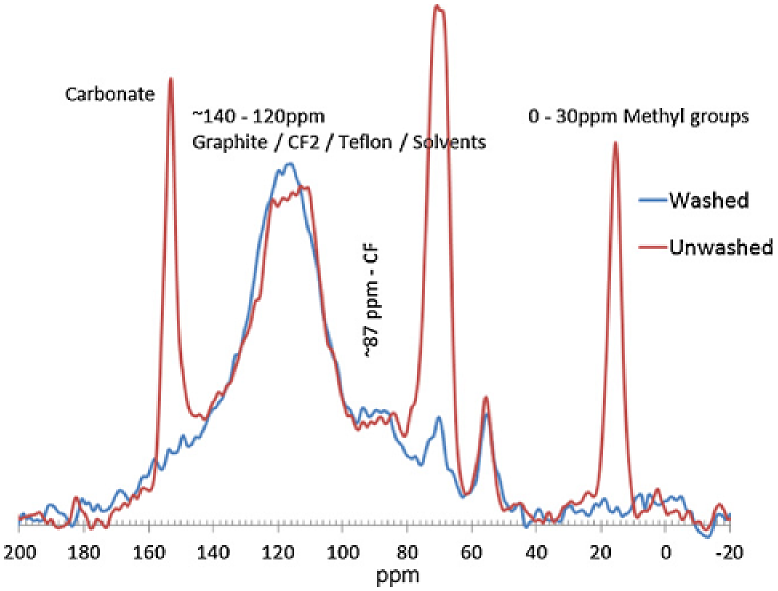

Figure 4.3.15: ^{13}C MAS NMR spectra of Hunter 80% discharged F series..

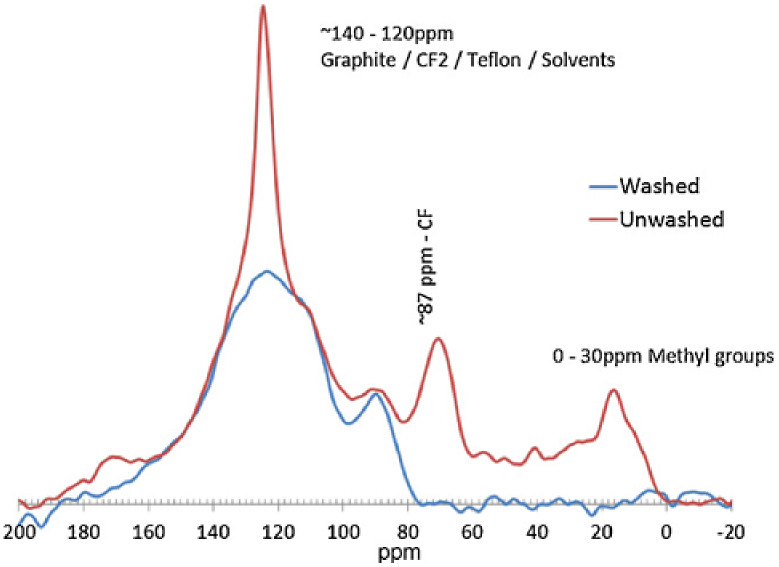

Figure 4.3.16: ^{13}C MAS NMR spectra of Hunter 46% discharged G series..

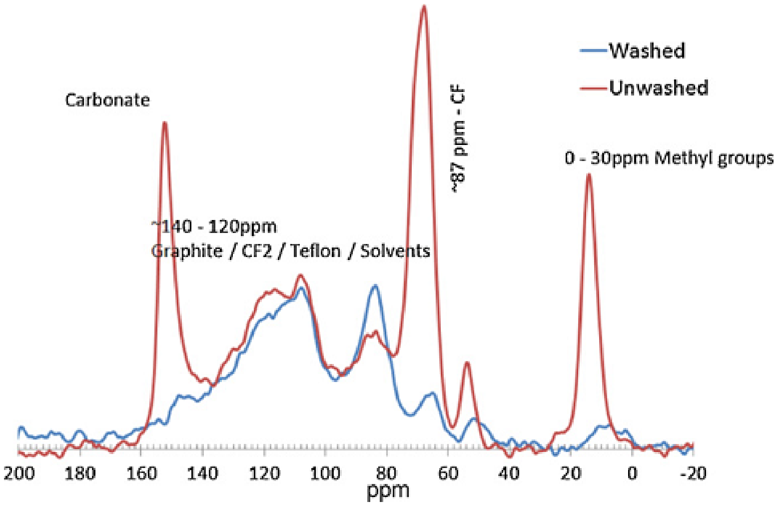

Figure 4.3.17: ^{13}C MAS NMR spectra of Hunter 46% discharged C series..

4.4 Conclusions

^{19}F and ^{13}C NMR of electrochemically lithiated CF_x of different morphologies reveal largely similar behavior of LiF formation. Unlike chemically lithiated samples[6] the semi-ionic CF consumption is faster than covalent CF in electrochemically discharged cells. Samples undergoing relatively fast discharge exhibit higher LiF contents at the corresponding DoD values, most likely due to inhomogeneity. An important observation was that no metastable compounds detectable by ^{19}F or ^{13}C NMR were found in the fast discharged samples. ^{13}C MAS NMR data also showed some similar behavior of carbon formation. For all three types of CF_x, however one significant observation was the consistent appearance of sp^3 bonded carbon in the F series at higher DoD values. Given the superior performance of the F series at higher DoD values, it is surmised that there is a structural rearrangement of the carbon lattice involving sp^3 bonded carbon which stabilizes the material at high DoD levels. Supporting evidence for the stability of F-type CF_x comes from both ^{7}Li and ^{19}F T_1 measurements which suggest that LiF formed upon discharge is excluded from the structure of the material more readily than in the C and G series.

Chapter 5

Layered Polymer Dielectrics

5.1 Introduction

Capacitors play a vital role almost universally in electronics. They are commonly used in filtering, noise reduction and pulsed power production systems. With the rapid development phase of electronics, it is extremely important to develop new capacitors with high performance in small packages. Replacing batteries with capacitors in some devices to achieve high charge/discharge rates, i.e. the global trend of electronics miniaturization and military interests in different types of weapons and electronic transport applications[3], is a large venue for scientific research.

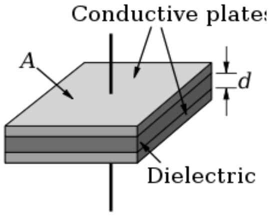

Figure 5.1.1: Parallel plate capacitor model.

The simplest capacitor consists of two parallel conductive plates separated by a dielectric with permittivity ϵ and the plates considered to extend uniformly over an area A. Assuming that the width of the plates is much greater than their separation d, the capacitance C, is given by,

$$C = \frac{\epsilon A}{d} \tag{5.1.1}$$

The capacitance is therefore greatest in devices made from materials with a high permittivity, large plate area, and small distance between plates. However the maximum energy storage using V_d as the dielectric (breakdown) strength per unit distance is,

$$E = \frac{1}{2}\epsilon A d V_d^2 \tag{5.1.2}$$

As shown in the Eqn. 5.1.2, the storage energy is directly related to the dielectric material as the dielectric constant and the square of the dielectric strength V_d. In order to maximize the charge that a capacitor can hold, the dielectric material needs to have as high a permittivity and breakdown voltage as possible.

Polymer dielectrics are ideal materials for advanced capacitor development because they are inexpensive, light weight, and easy to produce commercially. In addition, polymers generally have high breakdown strengths, and are not prone to sudden catastrophic failure such as cracking from thermal or physical shock like ceramic capacitors. Unfortunately, polymers with high dielectric constants do not necessarily have high dielectric breakdown strengths. It is in this regard that a great deal of research is carried out with mixtures of different types of polymers (via blending and layering or stacking) for better performance.

Attempts at increasing the dielectric constant of a polymeric mixture by blending-in a polymer of higher dielectric constant, more often than not, result in an overall lowering of the breakdown voltage. It can be understood that the newly created interfacial area (parallel to the applied e-field) becomes more susceptible to dielectric breakdown. Hence an increase of dielectric breakdown solely from blending cannot be expected. However, significantly improvements have been made towards increasing breakdown strength by using the stacking technique (i.e. layering of polymers PMMA[1] with PC[2])[20].

It has been recognized for some time that when two polymers are brought into intimate contact, the interface between them is not perfect sharp. Highly localized mixing of polymer chains creates an

---

[1] PMMA (Poly methyl methacrylate) possesses good thermal and mechanical stability, high electrical resistivity, and a suitably large dielectric constant. These qualities taken along with its thin film process-ability, make PMMA an ideal candidate as a dielectric layer in organic electronics.

[2] PC (Polycarbonate) is mainly used in electronic applications for its collective safety features. Being a good electrical insulator, in addition to having high heat resistance and good flame retardant properties, it serves as a highly stable dielectric. In this way, it points towards the design of highly tolerant capacitors capable of performing over a wide temperature range without degradation.

interphase region[4]. In this project of polymers suitably stacked for enhanced dielectric breakdown, NMR spectroscopy has been employed to investigate any interfacial interaction between polymer layers. The aim of these measurements is to find spectroscopic evidence of microstructural phenomena along the PC/PMMA interfaces that may be related to the enhanced dielectric properties of these layered materials.

5.2 Experiments

Samples were obtained from the research group of Prof. Eric Baer at *Case Western Reserve University, Cleveland.* Alternating films of PMMA (poly methyl methacrylate) and PC (polycarbonate) were prepared with different numbers of layers and thicknesses. In order to improve the film's surface smoothness and protect it from damage, a sacrificial polyethylene (PE) surface layer was added to the both external sides of the PMMA/PC stack (the PE layers were removed before measurements). Pure non-layered 50 μm thick PC and PMMA films were studied for comparison.

Composition (PC/PMMA)	Total film thinkness (μm)	PC layer thinkness (nm)	PMMA layer thinkness (nm)
50/50	50	1600	1600
	12	375	375
	3	110	110
70/30	50	2220	980
	12	530	230
	3	150	70
30/70	50	980	2220
	12	230	530
	3	70	150

Table 5.1: Microlayered PC/PMMA with 32 layers.

Composition (PC/PMMA)	Total film thinkness (μm)	PC layer thinkness (nm)	PMMA layer thinkness (nm)
50/50	220	220	220
	120	120	120
	50	50	50
	24	24	24
	12	12	12

Table 5.2: Microlayered PC/PMMA with 1024 layers.

First, the PE layers were removed by applying masking tape onto each side of the sample. Next, with the masking tape bound to the PE, the pure PMMA/PC layered samples were obtained by carefully peeling away the masking tape. The layered PMMA/PC films were cut in to small pieces and packed in to 3.2 mm zirconia rotors under ambient atmosphere.

^{13}C MAS NMR measurements were performed on a Varian 300 MHz spectrometer at a spinning rate of 7 kHz. ^{1}H cross polarization (CPMAS sequence) was employed to significantly reduce the experimental time typically encountered due to the low natural abundance of ^{13}C. All the measurements are referenced to tetramethylsilane (TMS) at 0 ppm.

5.3 Results and Discussions

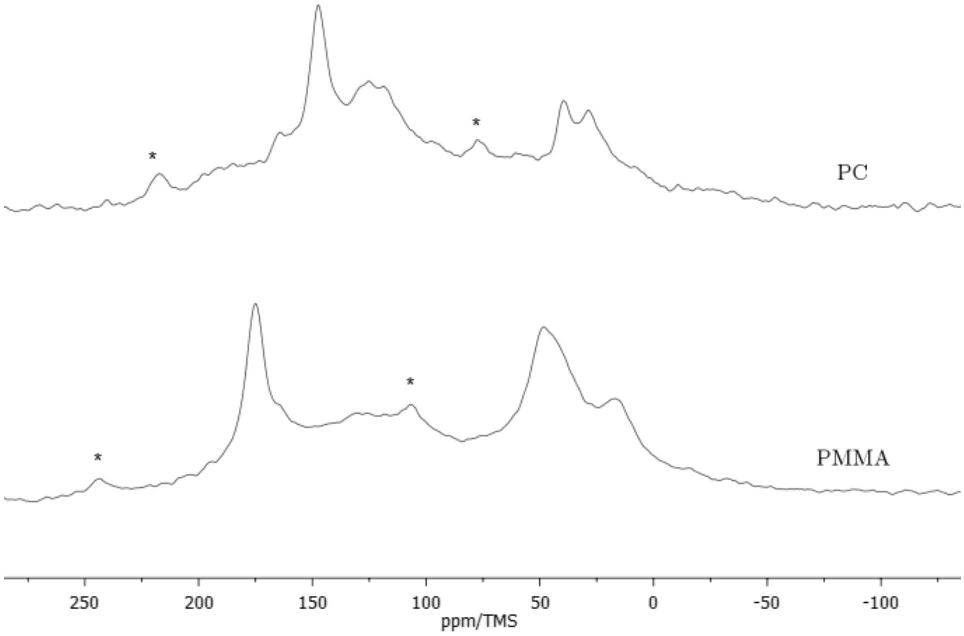

Figure 5.3.1: ^{13}C CPMAS NMR spectra of 50 μm PC and PMMA spinning at 7 KHz. * denotes sidebands. Scale is referenced to TMS.

^{13}C CPMAS NMR spectra of 50 μm PC and PMMA controls are shown in Fig. 5.3.1. The two distinct methyl carbon environments (CH_3 and $C(CH_3)_2$) of PC are indicated by the two peaks around 43 ppm and 32 ppm respectively. Two different chemical environments of ring carbons are visible at 121 ppm and 128 ppm and the carboxylic (C=O) carbon is found at 150ppm. The CH_3 of PMMA can be found at 15 – 20 ppm followed by CH_2 at 45 – 55ppm and the carboxylic carbon is located around 175ppm.

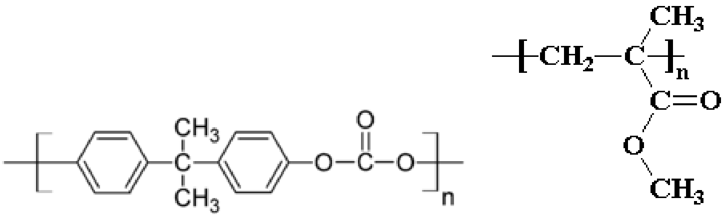

Figure 5.3.2: PC (left) and PMMA (right) chemical structures.

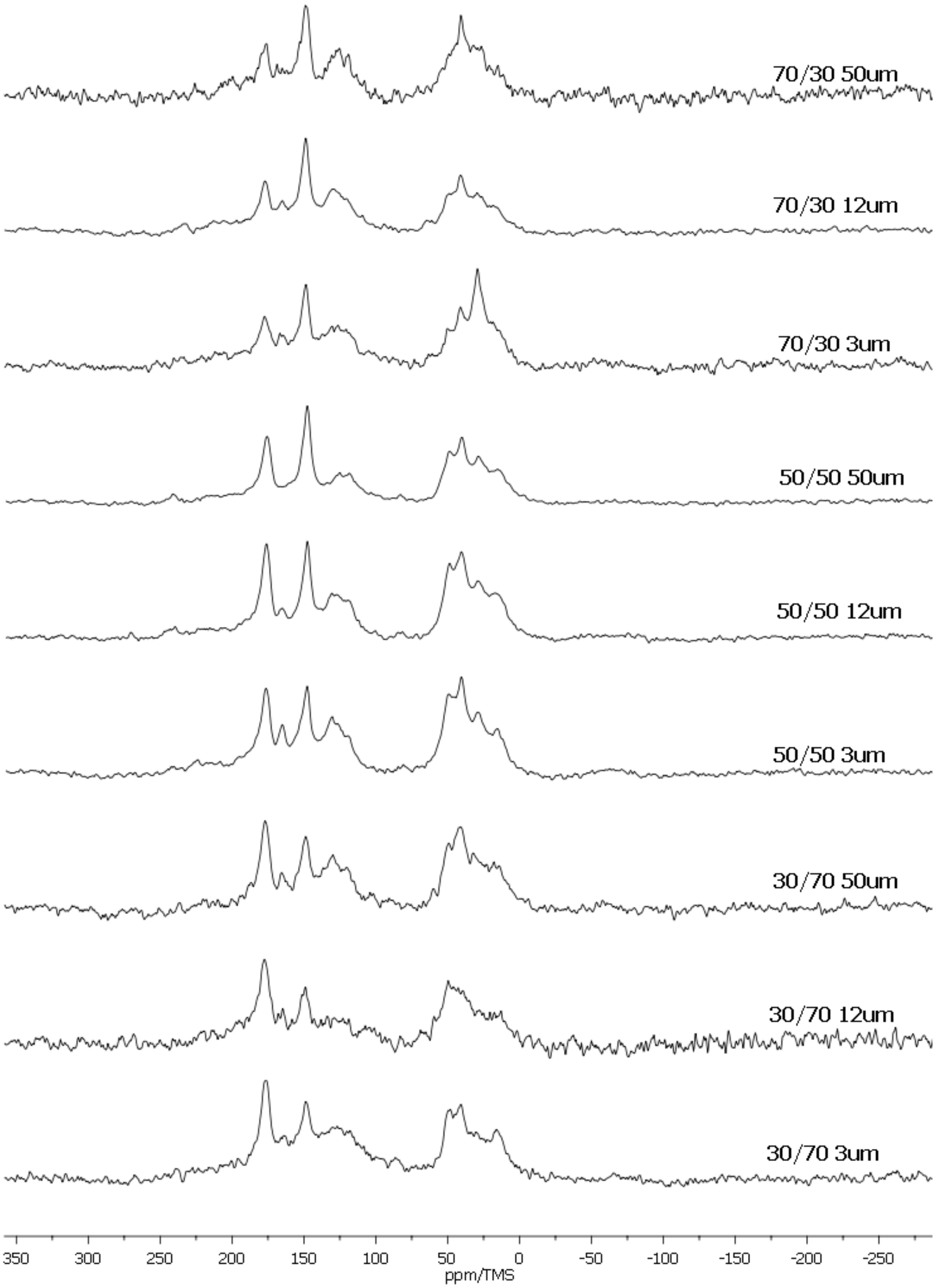

Figure 5.3.3: ^{13}C CPMAS NMR spectra of 32 layers PC/PMMA polymers. The first number denotes the PC composition followed by PMMA composition and the total thickness. Ex. first spectrum (top) is a 50 μm thick layers with 70/30 PC/PMMA composition.

Some spectra have considerably low SNR (signal to noise ratio), although each sample was signal averaged $\sim$ 24 hours. The PC and PMMA controls were run at relatively shorter periods of time for similar SNR. ^{13}C CPMAS NMR spectra of samples comprised of 32 layers (with thicker polymer components) and 1024 layers (thinner polymer components) are illustrated in Fig. 5.3.3 and 5.3.4 respectively. These spectra are clearly superposition spectra of the PC and PMMA components, i.e., the peaks at 175 ppm and 150 ppm are attributed to carboxylic (C=O) of PMMA and PC respectively. The small peak between those two peaks is due to some residual of the PE protecting film or the background. ^{13}C CPMAS NMR of the pure PE film shows a similar peak at the same position (not included in the figure). Again the two distinct methyl carbon environments (CH_3 and $C(CH_3)_2$) of PC are indicated by two peaks around 43 ppm and 32 ppm respectively, as observed for the PC control. CH_3 and CH_2 groups are responsible for the cluster of peaks from 15ppm to 55ppm.

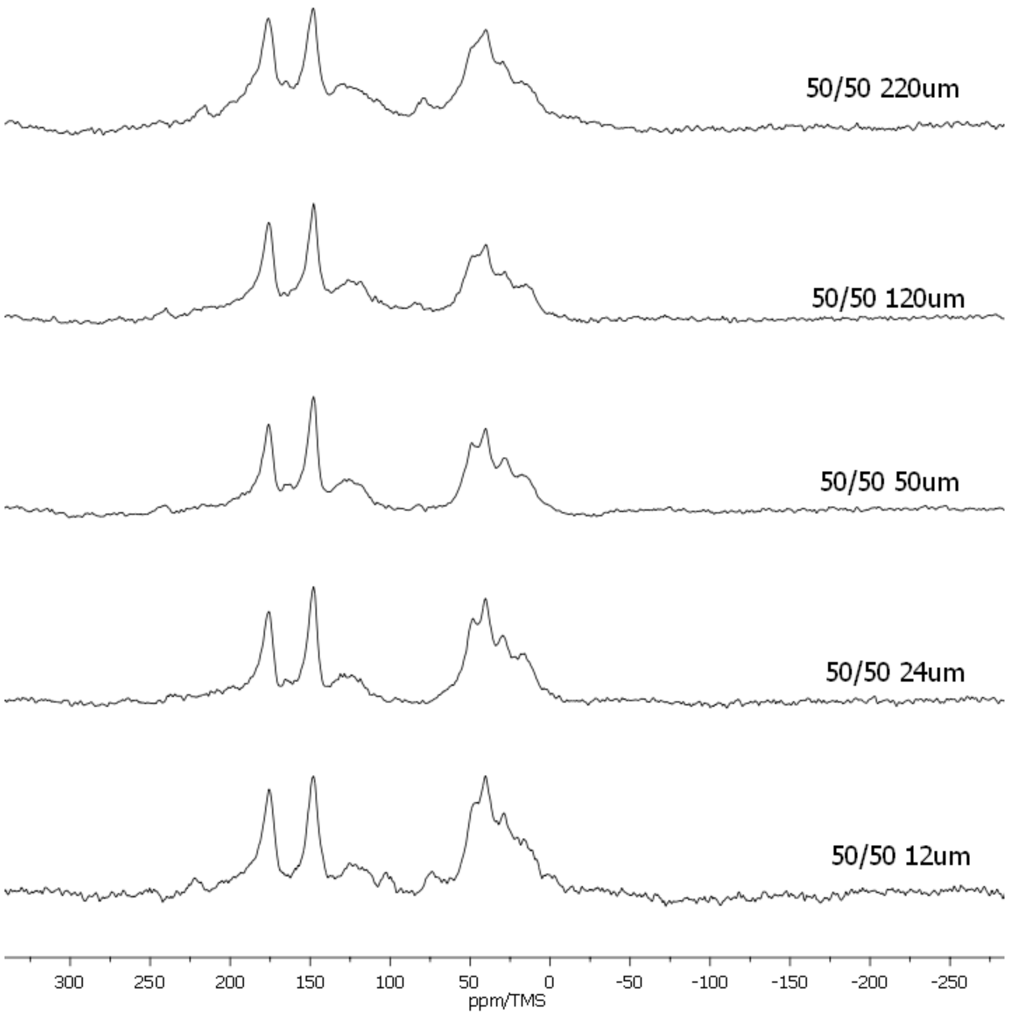

Figure 5.3.4: ^{13}C CPMAS NMR spectra of 1024 layers PC/PMMA polymers. The first number denotes the PC composition followed by PMMA composition and the total thinkness. Ex. first sepctrum (top) is a 220 μm think layers with 50/50 PC/PMMA compistion.

Direct comparison between samples of 32 layers and 1024 layers is shown in Fig. 5.3.5. Both spectra have the same number of scans and were obtained under similar conditions. It is seen that both spectra are identical in every respect, besides the residual PE peak around 165 ppm for the 1024 layer sample. In this regard, no spectroscopic differences have been observed between samples comprised of 32 versus 1024 layers.

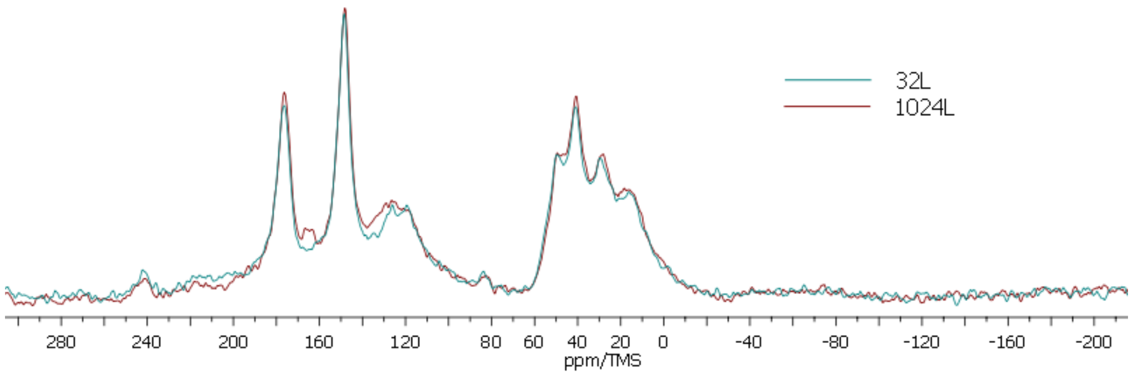

Figure 5.3.5: ^{13}C CPMAS NMR of 32 layers vs. 1024 layers of 50/50 PC/PMMA 50 μm layers.

5.4 Conclusions

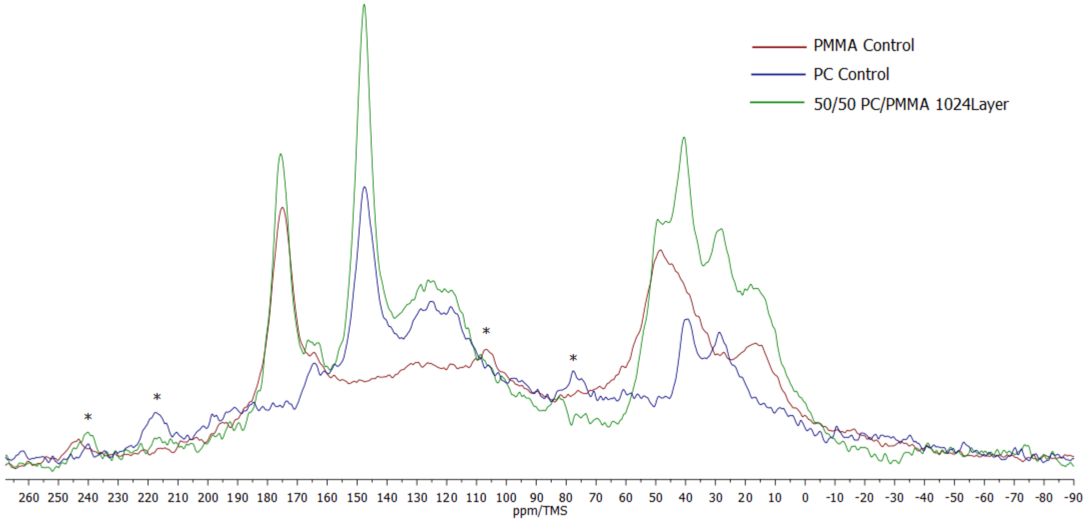

Figure 5.4.1: ^{13}C CPMAS NMR spectra of 50um PC, PMMA controls and 50/50 PC/PMMA 1024 layers polymer.

In spite of number of the layers, the NMR spectra of layered polymers can be interpreted in terms of superposition PC and PMMA components. No additional features were observed other than those observed in the controls (Fig. 5.4.1). It is observed, from these NMR spectroscopic results that there is no clear evidence (in NMR scale) of inter-molecular mixing between PC/PMMA at the interfaces.

Based on a rough assumption of a 0.1 nm interfacial mixing region between layers, one can estimate that ~3% of the sample could give a rise to new or shifted peaks in the 3 nm thick layered film. Unfortunately, data were obtained only for the 12 to 220 nm layers. Thus the detection of new peaks at the interface is somewhat less than 1% for the 12 nm sample, which according to our experience with the Varian spectrometer should still be detectable. We therefore conclude that the enhanced dielectric breakdown strength in the layered films arises from molecularly abrupt interfaces with no clear evidance of mixing.

Chapter 6

Thermoelectric (TE) Si/B and Si/P Alloys

6.1 Introduction

Considering the operation of high energy electronic devices (refrigerators, motors, air conditioners, etc.), a vast quantity of untapped natural heat is generated and discharged into the environment. Thermoelectric generation is an environmentally friendly technology which converts a portion of this unused heat, and in particular lower temperature heat, into electricity. This technology has been successfully demonstrated on a laboratory scale and in prototype commercial systems as well as spacecraft which operate at extraordinary distances where the Sun's light is too faint to power solar panels.

The increase in the price of crude oil accompanied by an increased awareness of environmental problems associated with global warming, resulted in an upsurge of scientific activity to identify and develop environmentally friendly sources of electrical power (green technology). Thermoelectric energy generation allows for an overall increase of the system's generating power density. This can be of greater importance, in determining the system's economic viability, than its conversion efficiency. Over the past ten years or so, effort has focused on developing thermoelectric generating systems which can recover waste heat from the human body, computer chips, automobile engines, and industrial utilities. In the near future, thermoelectric waste heat recovery may make a significant contribution, over a wide range of applications, in reducing fossil fuel consumption and global warming.

Conventional metallic thermocouples[1] are made from metal or metal alloys. They generate small voltages, typically tens of microvolts per degree temperature difference by the Seebeck effect. The Seebeck effect is the conversion of temperature differences directly into electricity and is named for German physicist Thomas Johann Seebeck, who, in 1821 discovered that a compass needle would be deflected by a closed loop formed by two metals joined in two places, with a temperature difference between the junctions.

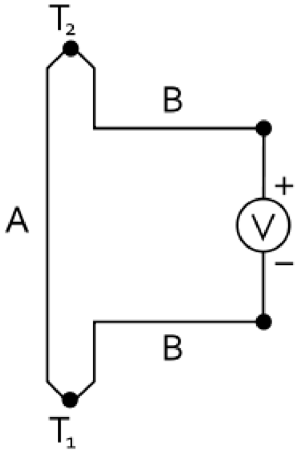

Figure 6.1.1: Diagram of the circuit on which Seebeck discovered the Seebeck effect. A and B are two different metals.

The voltage V developed can be approximately[2] given by,

$$V = (\alpha_B - \alpha_A) \cdot (T_2 - T_1) \tag{6.1.1}$$

Where α_A and α_B are the thermopowers/Seebeck coefficient of metals A and B as a function of temperature and T_1 and T_2 are the absolute temperatures of the two junctions. The Seebeck coefficients are non-linear as a function of temperature, and depend on the conductors' absolute temperature, material, and molecular structure. Conveniently the efficiency can be expressed as a function of the temperature over which it is operated and a so called 'goodness factor' or thermo-

---

[1] A thermocouple is a junction between two different metals that produces a voltage related to a temperature difference.

[2] If the Seebeck coefficients are effectively constant for the measured temperature range

electric figure-of-merit of the thermocouple material Z[21].

$$ZT = \frac{\alpha^2 \sigma T}{\kappa} = \frac{\alpha^2 T}{\rho\kappa} \tag{6.1.2}$$

Where σ is the electrical conductivity, ρ is the electrical resistivity, and κ is the total thermal conductivity ($\kappa = \kappa_L + \kappa_E$, the lattice and electronic contributions, respectively). The power factor, $\alpha^2\sigma T$, is typically optimized in narrow-gap semiconducting materials as a function of carrier concentration, through doping, to give the largest ZT. High-mobility carriers are most desirable, in order to have the highest electrical conductivity for a given carrier concentration. The ZT for a single material is somewhat meaningless, since an array of TE couples is utilized in a device or module. Ignoring parasitic contributions that reduce the device performance, such as contact resistance and radiation effects, the resulting figure of merit for the couple of semiconductor materials is given by[21],

$$ZT = \frac{(\alpha_p - \alpha_n)^2 T}{\left[(\rho_n\kappa_n)^{1/2} + (\rho_p\kappa_p)^{1/2}\right]} \tag{6.1.3}$$

The best TE materials currently used in devices have $ZT \sim 1$. This value has been a practical upper limit for more than 30 years, yet there are no theoretical or thermodynamic reasons for $ZT \sim 1$ as an upper barrier. As seen from Eqn. 6.1.3, ZT may be increased by decreasing κ or by increasing either α or σ at a given temperature.

Different types of semiconductor materials have been studied by different research groups. Among different systems, ball-milled and doped (P, B) nano-silicon, which shows great promise towards higher Seebeck coefficients and higher efficiencies, is being developed for these applications. The essential idea, originally conceived jointly by Prof. Mildred Dresselhaus at *MIT* and Prof. Richard Kaner at *UCLA*, is the following. Most materials that have high σ also possess high κ, so the goal is to maintain a reasonably high σ while disrupting the thermal transport through phonon scattering. Such a scheme was realized by using degeneratively (heavily) doped Si, which is metallic, and disordering it in a planetary mill (i.e. ball milling). With the proper amount of annealing it was found that enough electrical conductivity could be regained while still suppressing the thermal conductivity. In this project, ball-milled nano-silicon samples were investigated by NMR in order to understand the local structures surrounding silicon and the dopants B and P. Comparisions will be made between ball milled and standard crystalline (wafer) materials.

6.2 Experiment

Nano-silicon samples were obtained from the lab of Prof. Richard Kaner at UCLA (*University of California, Los Angeles*). Samples were placed in two categories depending upon the preparation (ball-milled and dopant reset) methods. Ball-milled material, both undoped and B or P doped were prepared by high energy ball-milling of the starting elements. The dopant reset procedure consisted of thermal annealing in several steps until the desired electrical and thermal properties were obtained. Except one sample (NSU0224, which is un-doped) each was doped with 1% or 2% phosphorus or boron.

Supplier symbol	Doping level (Atomic %)
NSU0224	0%
NSN3224	1% P
NSN3136	2% P
NSP0524	1% B
NSP0150	2% B

Table 6.1: Doping levels of Ball milled nano-silicon samples.

Supplier symbol	Doping level (Atomic %)
NSN3224	1% P
NSN3136	2% P
NSP07	2% B

Table 6.2: Doping levels of Dopant reset nano-silicon samples.

Since samples are air sensitive, they were delivered in air-tight packages. All ball milled samples were finely powdered, whereas the dopant reset samples were mixtures of little pieces (in a scale of less than a millimeter) and powder. Samples were opened and 3.2mm zirconia rotors were packed in an argon-filled glove box.

Three silicon-wafers, received from a commercial source (donated by *Siliconwafersubstrate.com*) were used to obtain base measurements for comparison. Of these samples, one wafer was un-doped, the other two were doped with 0.003 – 0.012% P and 0.06 – 0.26% B respectively. The doping levels were determined by use of the resistivity data provided by the manufacturer. Wafers were crushed thoroughly into a mixture of little pieces (in a scale of less than a millimeter) and a powder. Then the mixture was packed in 3.2mm zirconia rotor for NMR measurements. ^{29}Si, ^{31}P and ^{11}B MAS NMR experiments were performed on a 300MHz Varian Direct S spectrometers with spinning speeds 10 – 15 kHz. Single pulse sequences were used for all the measurements: 3.5us pulse-widths with 300s recycle delays for ^{29}Si, 2.3us with 3s recycle delays for ^{31}P and 2.5us with 2s recycle delay for ^{11}B. The respective reference compounds are TMS (^{29}Si at 59.9 MHz), H_3PO_4 (^{31}P at 122.0MHz) and $LiBF_4$ (^{11}B at 96.7MHz).

6.3 Results and Discussion

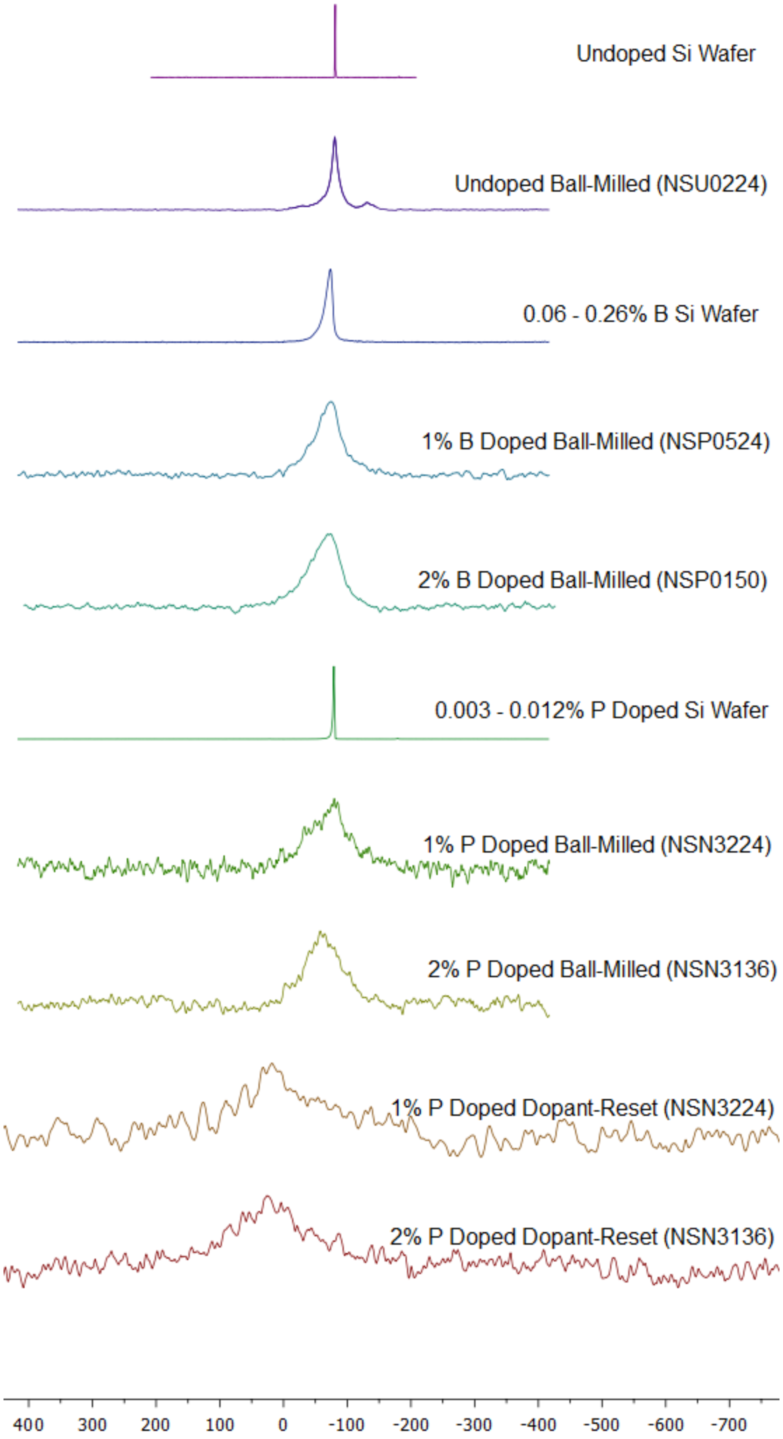

Figure 6.3.1: ^{29}Si MAS NMR spectra of Ball milled and Dopant reset samples.

In general each sample was signal averaged for 24 – 48 hours due to weak SNR. Dopant reset samples showed considerably lower SNR than ball milled ones with the similar number of averaging cycles. Moreover, dopant reset samples were not very stable at spinning above 7 - 10 kHz. The reason could be the eddy current generated due to the flake nature of the samples unlike the powder nature of ball-milled samples.

^{29}Si MAS NMR spectra are shown in Fig. 6.3.1. No side band is observed in any spectrum. The sharp peak around -80ppm of the crystals are assigned to crystalline tetrahedral Si-Si environment as expected for highly ordered materials. This result is consistant with studies of cystalline silicon published by other authors[11]. Amorphous bulk silicon in non-crystalline samples resonates at -81ppm[12]. In addition, aging can grow oxygenated species such as Si-O, Si-O-Si[16]. The weak peak of un-doped ball-milled sample (NSU0224) around -100ppm may be due to Si-O bonds[12]. Defects, broken bonds and other disordered nature are expressed by broadening of the ^{29}Si resonance in ball-milled and dopant reset samples because in amorphous materials containing a distribution of chemical bond angles and/or lengths, the resulting chemical shift dispersion cannot be narrowed by MAS. Furthermore No siginificant difference such as chemical shift or line-width change is observed between the doping levels from 1% to 2% in both P and B doped ball-milled and dopant reset samples.

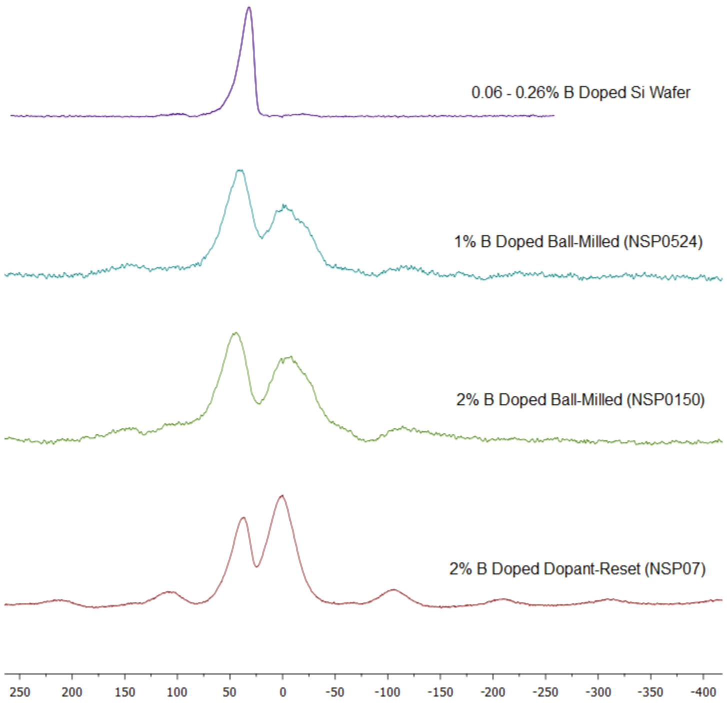

Figure 6.3.2: ^{11}B MAS NMR spectra of Ball milled and Dopant reset samples.

^{11}B MAS NMR spectra are shown in Fig. 6.3.2. The reference wafer exhibits a single peak assigned to tetrahedrally coordinated B, as is expected for the dopant ion. An unexpected second site appeared in all the ball milled and dopant reset ^{11}B spectra. ^{11}B is a quadrupole nucleus and if these two peaks are quadrupolar splittings, the separation between them should be inversely propotional to the external magnetic field. Therefore the same sample was investigated in a higher magnetic field (500 MHz vs. 300MHz) and no reduction in the splitting separation was observed and hence the second peak was assigned to a second site not associated with substitutional doping. The ratio of the two sites is very similar in both 1% and 2% ball milled samples. Moreover no siginificant difference such as chemical shift or line-width change is observed between the doping levels from 1% to 2% in both P and B doped ball-milled and dopant reset samples, similar to ^{29}Si MAS NMR.

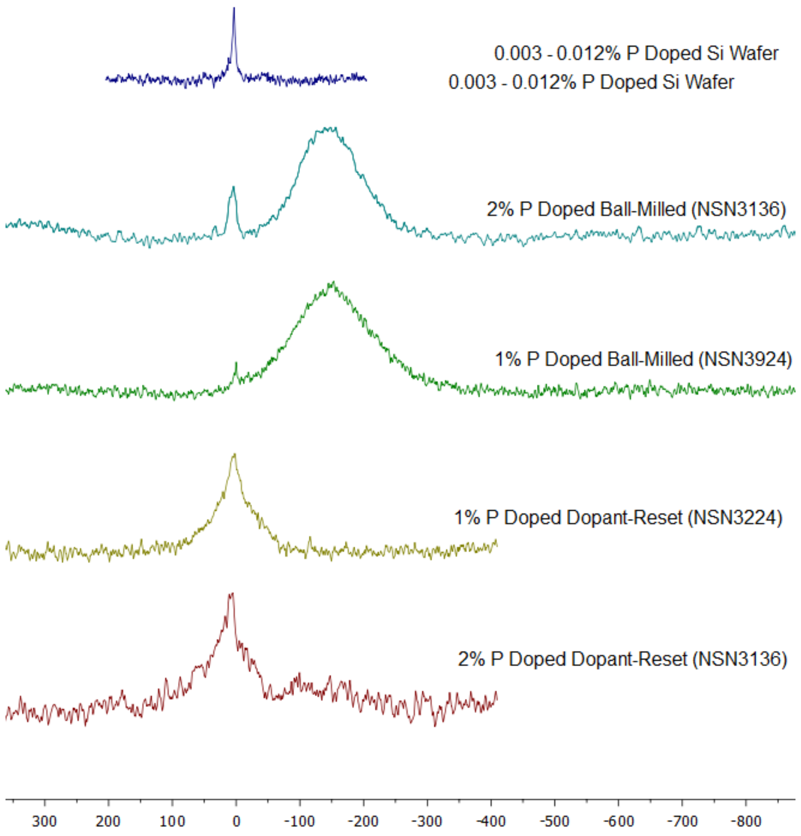

Figure 6.3.3: ^{31}P MAS NMR spectra of Ball milled and Dopant reset samples.

The ^{13}P signal (Fig. 6.3.3) is very weak compared to ^{11}B and ^{29}Si NMR. The weak peak visible in all spectra near 0 ppm is assigned to tetrahedrally coordinated P (i.e as in substitional doping). ^{31}P NMR chemical shifts of the six P sites in SiP typically range from -140 to -240ppm and two crystallographically equivalent three coordinated P are located around -143.6 and -152.6 ppm[15]. Therefore the large intensity centered at $\sim$ -140 ppm in the ball-milled samples is assigned to SiP-like regions, implying that the P is not uniformley distributed. However, upon annealing, this peak is suppressed and the substitional one grows.

6.4 Conclusions

Solid state ^{29}Si, ^{11}B and ^{31}P MAS NMR have been employed to investigate the micro-structural changes that occurred in ball milling and dopant-reset sample preparation methods. A number of differences were observed. Mainly, two B sites were observed in ball milled and dopent reset samples. One is four coordinated B and other one may be three coordinated B similar to the three coordinated P. Also the disordered nature, as judged by the NMR linewidths, remains in dopant reset samples compared to ball-milled ones and no siginificant difference is observed between the doping levels from 1% to 2% in both P and B doped ball-milled and dopant reset samples. Both four coordinated and three coordinated P sites were also observed in the ball milled samples. The dopant reset is apparently successful in suppressing the non-substitional site, thus implying an increased doping efficiency.

Chapter 7

Electrolyte Breakdown Products in the SEI of Li Ion Batteries

7.1 Introduction

Typical commercial lithium-ion batteries use a lithium transition metal oxide as the cathode, a carbonaceous material as the anode and an organic electrolyte based on a solution of a lithium salt in a mixture of two or more organic solvents. When in contact with liquid and polymer electrolytes, lithium (for lithium metal batteries) or lithiated graphite (for lithium ion batteries) are thermodynamically unstable toward the solvents and salts and reacts to form a passivating film coating that slows the corrosion of the anode. This layer, known as SEI (solid electrolyte interphase) formed instantaneously upon contact of the anode with the solution, consists of insoluble and partially soluble reduction products of electrolyte components. The electron-tunneling range is determined by the thickness of the freshly formed layer. The layer acts as an interphase between the metal and the solution and has the properties of a solid electrolyte with high electronic resistivity. The SEI determines the safety, power capability, morphology of lithium deposits, shelf life, and cycle life of the battery. Therefore it is very important to study the nature of the SEI in order to make improvements on battery performance.

Solid state NMR has been employed in this ongoing project to identify the composition of the SEI. Due to the unique quantitative nature of NMR, it provides additional information that complements other spectroscopic methods such as XPS (xray-photoelectron spectroscopy) and FTIR (Fourier transform infrared spectroscopy). Multinuclear (^{7}Li, ^{19}F, ^{31}P) MAS NMR studies of SEI formation on both positive ($LiNi_{0.8}Co_{0.2}O_2$) and negative (meso-carbon micro-beads graphite known as MCMB) electrodes have been performed on materials harvested from Li ion cells subjected to an accelerated aging protocol. Accelerated Aging is commonly used in the battery industry to speed up the deleterious processes in a cell. The Accelerated Aging process is based on the relationship of temperature and reaction rate where an increase in temperature increases the reaction rate and is approximated by the Arrhenius equation.

7.2 Experiment

23 sets of cells were used for this study. Different amounts and combinations of DTFEC, TFEMC, TPP and TPPi[1] with $LiPF_6$ were used as the electrolyte. Moreover, 5-10 wt% of PVdF (Polyvinylidene fluoride) was used as a binder in the electrodes. Each cell group was cycled under an accelerated aging protocol at the Jet Propulsion Lab (JPL) and provided to us by Dr. Marshall Smart. Each group has a different history and all cells in a group have identical histories. The batches CH01 - CH05 have the least amount of cycling (i.e., formation and only a couple of discharges at various temperatures); whereas the other batches generally have much more extensive cycling and some have been cycled at high temperature (i.e., under stressful conditions). Generally electrodes were harvested when the cells are about $\sim$ 3.80V OCV (open circuit voltage). Samples and associated treatment protocols are listed below,

---

[1] DTFEC = di-2,2,2-trifluoroethyl carbonate, TFEMC = 2,2,2-trifluoroethyl methyl carbonate, TPP = triphenyl phosphate, TPPi = triphenyl phosphite, EC = ethyl carbonate, EMC = ethyl methyl carbonate, VC = vinyl carbonate.

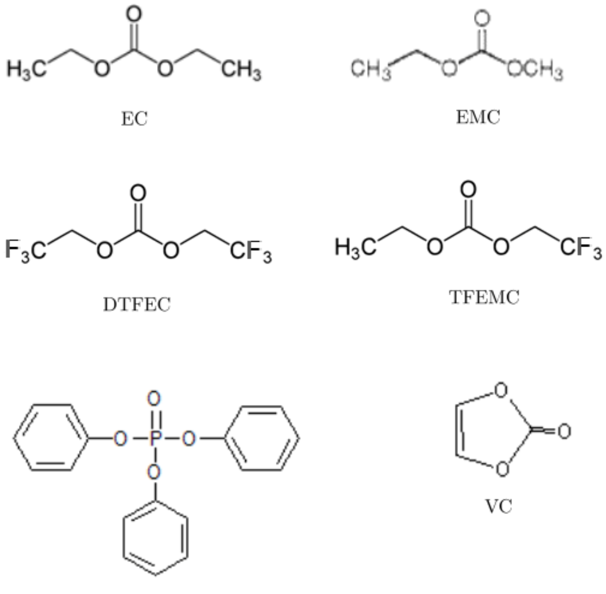

EC

EMC

DTFEC

TFEMC

TPP

VC

Figure 7.2.1: Chemical structures of the solvent EC, EMC and additives.

Sample	Protocol
• GB01: 1.00 M $LiPF_6$ EC+EMC (20:80 v/v %) • GB03: 1.00 M $LiPF_6$ EC+EMC+DTFEC+TPP (20:50:20:10 v/v %) • GB04: 1.00 M $LiPF_6$ EC+EMC+DTFEC+TPP (20:30:40:10 v/v %) • GB05: 1.00 M $LiPF_6$ EC+EMC+TPP (20:70:10 v/v %)	• Formation Cycling (5 Cycles at 23^{o}C) – C/16 charge rate to 4.10V (C/100 taper current cut-off) – C/16 discharge rate to 2.75V • Discharge rate characterization with room temperature charge ($\sim$ 11 cycles) – Range of temperatures = 23^{o}, 0^{o}, -20^{o}, and -30^{o}C • Discharge rate characterization with low temperature charge ($\sim$ 20 cycles) – Range of temperatures = 23^{o}, 0^{o}, -10^{o}, -20^{o}C, and -30^{o}C – Four discharge currents (25mA, 50 mA, 100mA, and 150 mA) – Two charge rates (25 mA and 50mA) – Four cycles at each temperature – Test can be strenuous if lithium plating is observed • Room temperature cycle life test ($\sim$ 100 cycles) – 100% DOD cycling – $\sim$ C/16 charge rate to 4.10V (C/100 taper current cut-off) – $\sim$ C/16 discharge rate to 2.75V

Sample	Protocol
• CK01: 1.00 M $LiPF_6$ EC+EMC (20:80 v/v %) • CK02: 1.00 M $LiPF_6$ EC+EMC+TPPi (20:70:10 v/v %) • CK03: 1.00 M $LiPF_6$ EC+EMC+TPPi (20:60:20 v/v %) • CK04: 1.00 M $LiPF_6$ EC+EMC+TPPi (20:75:5 v/v %) w/ 1.5 % VC	• Formation Cycling (5 Cycles at 23^{o}C) – C/16 charge rate to 4.10V (C/100 taper current cut-off) – C/16 discharge rate to 2.75V • Discharge rate characterization with room temperature charge (∼ 10 cycles) – Range of temperatures = 23^{o}, -20^{o}, -30^{o}C, -40^{o}C, and -60^{o}C • Discharge rate characterization with low temperature charge (∼ 8 cycles) – Range of temperatures = 23^{o} and -20^{o}C – Four discharge currents (25mA, 50 mA, 100mA, and 150 mA) – Two charge rates (25 mA and 50mA) – Four cycles at each temperature – Test can be strenuous if lithium plating is observed • Room temperature cycle life test (∼ 100 cycles) – 100% DOD cycling at 23^{o}C – ∼ C/16 charge rate to 4.10V (C/100 taper current cut-off) – ∼ C/16 discharge rate to 2.75V

Sample	Protocol
• FP01: 1.0 M $LiPF_6$ FEC+EMC+TFEMc+TPP (20:50:20:10 v/v %) • FP02: 1.0 M $LiPF_6$ FEC+EMC+TPP (20:70:10 v/v %) • FP03: 1.0 M $LiPF_6$ EC+EMC+TFEMC+TPP (20:50:20:10 v/v %) • FP04: 1.0 M $LiPF_6$ FEC+EMC+TFEMC+TPP (20:50:20:10 v/v %) + 1.5% VC	• Formation Cycling (5 Cycles at 23^{o}C) – C/16 charge rate to 4.10V (C/100 taper current cut-off) – C/16 discharge rate to 2.75V • Discharge rate characterization with room temperature charge (18 cycles) – Range of temperatures = 23^{o}, 0^{o}, -10^{o}, -20^{o}C, -30^{o}, -40^{o}C, and -50^{o}C • Discharge rate characterization with low temperature charge ($\sim$ 20 cycles) – Range of temperatures = 23^{o}, 0^{o}, -20^{o}C, and -30^{o}C (Repeat of 23^{o}C) – Four discharge currents (25mA, 50 mA, 100mA, and 150 mA) – Two charge rates (25 mA and 50mA) – Four cycles at each temperature – Test can be strenuous if lithium plating is observed • Cycle life test at high temperature (60^{o}C) – 20 Cycles performed at high temperature (60^{o}C) – 100% DOD cycling – $\sim$ C/8 charge rate (50 mA) to 4.10V (C/100 taper current cut-off) – $\sim$ C/8 discharge rate (50mA) to 2.75V

Sample	Protocol
• HH01: 1.2M $LiPF_6$ in EC+EMC+MB (20:20:60 vol %) • HH02: 1.2M $LiPF_6$ in EC+EMC+MB (20:20:60 vol %) + 2% FEC • HH03: 1.2M $LiPF_6$ in EC+EMC+MB (20:20:60 vol %) + 4% FEC • HH04: 1.2M $LiPF_6$ in EC+EMC+MB (20:20:60 vol %) + lithium oxalate • HH05: 1.2M $LiPF_6$ in EC+EMC+MB (20:20:60 vol %) + 2% VC • HH06: 1.2M $LiPF_6$ in EC+EMC+MB (20:20:60 vol %) + 0.10M LiBOB	• Formation Cycling (5 Cycles at 23^oC) – C/16 charge rate to 4.10V (C/100 taper current cut-off) – C/16 discharge rate to 2.75V • Discharge rate characterization with room temperature charge (19 cycles) – Range of temperatures = 23^o, 0^o, -10^o, -20^oC, -30^o, -40^oC, and -50^oC • Discharge rate characterization with low temperature charge ($\sim$ 12 cycles) – Range of temperatures = 23^o, 0^o, and -20^oC – Four discharge currents (25mA, 50 mA, 100mA, and 150 mA) – Two charge rates (25 mA and 50mA) – Four cycles at each temperature – Test can be strenuous if lithium plating is observed • Cycle life test at high temperature (60^oC) – 20 Cycles performed at high temperature (60^oC) – 100% DOD cycling – $\sim$ C/8 charge rate (50 mA) to 4.10V (C/100 taper current cut-off) – $\sim$ C/8 discharge rate (50mA) to 2.75V • Cycle life test at high temperature (80^oC) – 20 Cycles performed at high temperature (80^oC) – 100% DOD cycling – $\sim$ C/8 charge rate (50 mA) to 4.10V (C/100 taper current cut-off) – $\sim$ C/8 discharge rate (50mA) to 2.75V

Sample	Protocol
• CH01: 1.0 M $LiPF_6$ EC+DEC+DMC (1:1:1 vol %) • CH02: 1.0 M $LiPF_6$ EC+EMC+TPP (20:75:5 vol %) + 1.5% VC • CH03: 1.0 M $LiPF_6$ + 0.15M LiBOB EC+EMC+TPP (20:70:10 vol%) • CH04: 1.0 M $LiPF_6$ + 0.05M LiBOB in EC+EMC+DMMP (30:55:15 wt %) • CH05: 1.0 M $LiPF_6$ EC+DMC+MB (1:1:3 wt %) + 1.5% VC	• Formation Cycling (5 Cycles at 23^{o}C) – C/16 charge rate to 4.10V (C/100 taper current cut-off) – C/16 discharge rate to 2.75V • Discharge rate characterization with room temperature charge (3 cycles) – Range of temperatures = 23^{o}, 0^{o}, and -20^{o}C • Discharge rate characterization at room temperature (4 cycles) – Temperatures = 23^{o}C – Four discharge currents (25mA, 50 mA, 100mA, and 150 mA) – Two charge rates (25 mA and 50mA)

1 M $LiPF_6$ in a mixture of EC: EMC (20:80 v/v %) was used as the baseline electrolyte. Variations of electrolyte solvents were included such as substitution of monofluoroethylene carbonate (FEC) for EC or addition of methyl butyrate (MB) to enhance low temperature performance. In addition, the effect of adding a fire retardant, triphenyl phosphate (TPP), to the electrolyte was evaluated.

For NMR measurements, the electrodes (both anode and cathode) were scraped off the current collector inside an argon filled glove-box. Each sample was packed into 1.6 mm rotors and spun at 39 kHz. NMR measurements were carried out on a Varian spectrometer with a 7.1T field strength. Aqueous lithium triflate (Lithium trifluoromethanesulfonate) solution was used as the chemical shift reference for ^{7}Li and $CFCl_3$ was used for the ^{19}F. A spin echo sequence with a 1.1μs $\pi/2$ pulse width and 10s recycle delay was employed for ^{7}Li and ^{19}F measurements. The same pulse sequence was used for ^{31}P MAS NMR with a recycle delay of 200s. ^{31}P chemical shifts were referenced to a H_3PO_4 solution.

7.3 Results and Discussion

Accumulation of about 50 transients for both ^{19}F and ^{7}Li MAS NMR were sufficient for good SNR. On the other hand, due to low SNR, ^{31}P MAS NMR measurements were signal averaged for longer periods of time (∼ 48 hours). Even with the high number of transients, some spectra still have considerably low SNR. GB01: 1M $LiPF_6$ EC+EMC (20:80 v/v%) is considered as the base line.

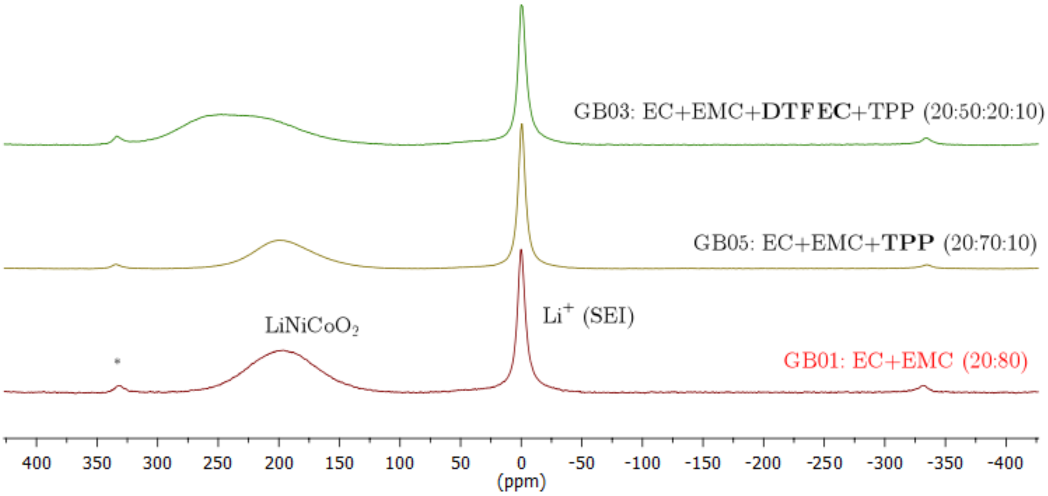

Figure 7.3.1: ^{7}Li MAS NMR spectra of the cathode GB series.

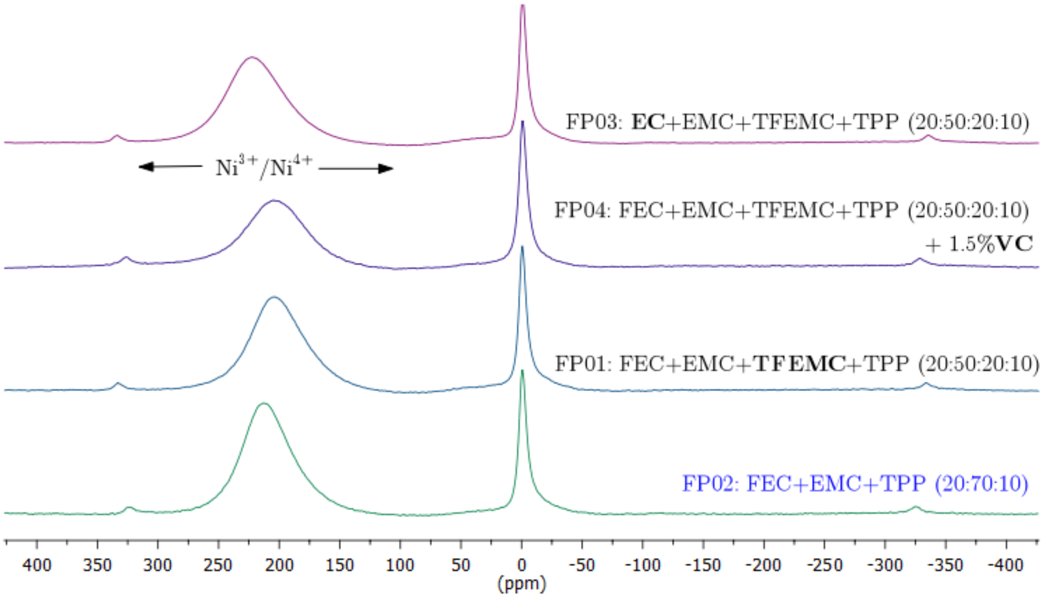

Figure 7.3.2: ^{7}Li MAS NMR spectra of the cathode FP series.

^{7}Li MAS NMR of the GB and FP cathode series are illustrated in Fig. 7.3.1 and 7.3.2 respectively. The peak around 0 ppm is attributed to irreversible Li$^+$ of the SEI and some dried electrolyte salt[22]. Clearly, there is little spectroscopic difference between samples of these two series. The broad feature centered at 200 ppm arises from Li$^+$ ions in the active cathode material. This relatively large shift is attributed to the presence of paramagnetic Ni^{3+} in the cathode. The integrated area under the peak is a measure of the reversible Li$^+$ content in the cathode (Table 7.2). FP02: 1.0 M LiPF$_6$ FEC+EMC+TPP shows the highest Li$^+$ content while GB05: 1.0 M LiPF6 EC+EMC+TPP has the lowest.

Sample	Li+ peak position (ppm)	Area ratio of the peaks at 200ppm to 0ppm
GB01: 1.00 M LiPF6 EC+EMC (20:80 v/v %)	197.4	1.00
GB03: 1.00 M LiPF6 EC+EMC+DTFEC+TPP (20:50:20:10 v/v %)	247.1	1.08
GB05: 1.00 M LiPF6 EC+EMC+TPP (20:70:10 v/v %)	197.6	0.59
FP01: 1.0 M LiPF6 FEC+EMC+TFEMc+TPP (20:50:20:10 v/v %)	202.7	1.76
FP02: 1.0 M LiPF6 FEC+EMC+TPP (20:70:10 v/v %)	211.0	2.00
FP03: 1.0 M LiPF6 EC+EMC+TFEMC+TPP (20:50:20:10 v/v %)	217.7	1.75
FP04: 1.0 M LiPF6 FEC+EMC+TFEMC+TPP (20:50:20:10 v/v %) + 1.5% VC	199.2	1.39

Table 7.2: Area ratios and peak positions of Li$^+$ at 200 ppm. The area is normalized to GB01.

The change in the chemical shift around 200ppm suggests that there is a mixed-valence Ni^{3+}/Ni^{4+} environment in addition to Ni^{3+}. The higher the Ni^{3+}/Ni^{4+} ratio implies the higher chemical shift. For example, GB03 has the highest Ni^{3+}/Ni^{4+} ratio.

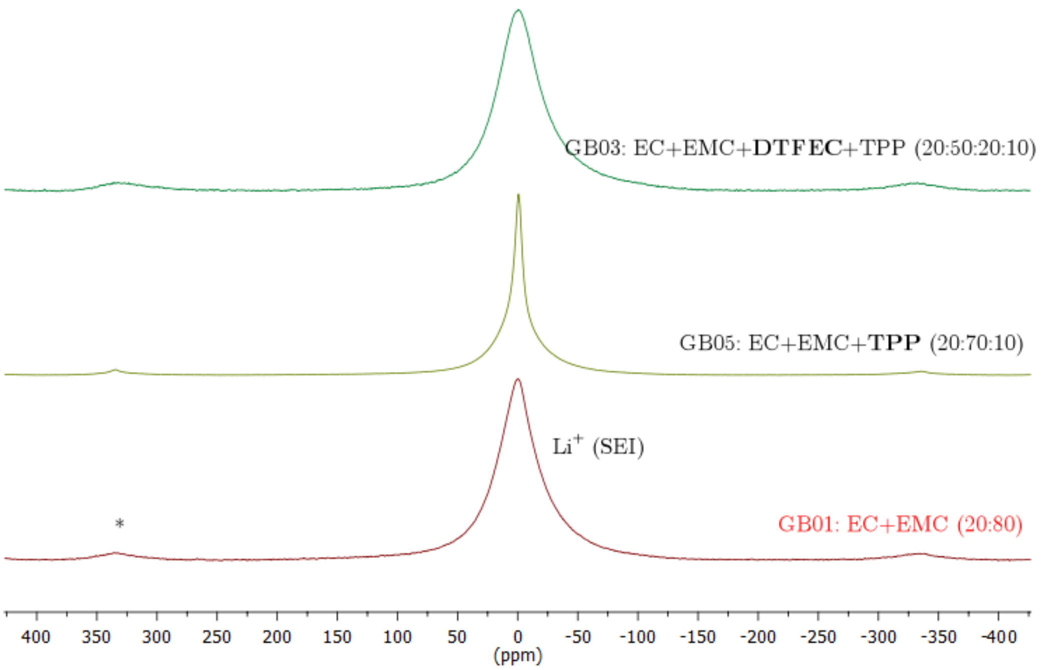

Figure 7.3.3: ^{7}Li MAS NMR spectra of the anode GB series.

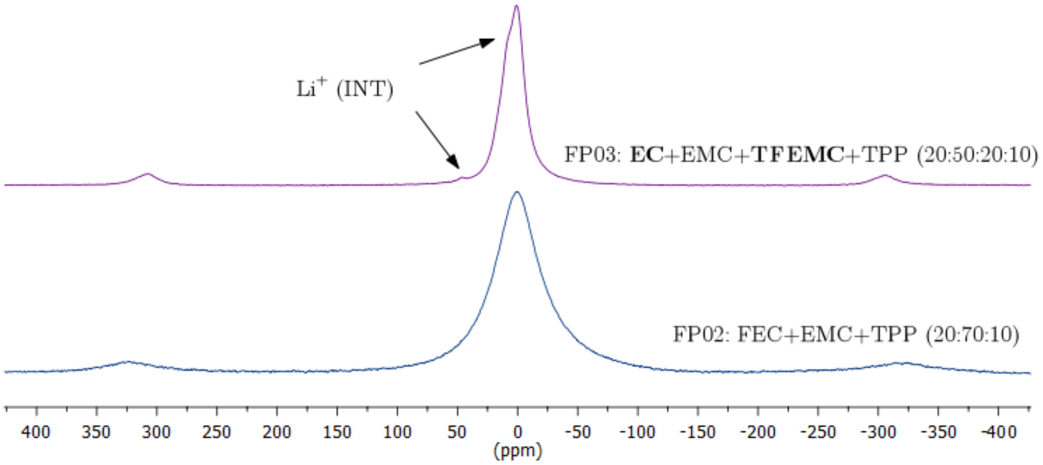

Figure 7.3.4: ^{7}Li MAS NMR spectra of the anode FP series.

^{7}Li MAS NMR of the GB and FP anode series are shown in Fig. 7.3.3 and 7.3.4 respectively. Again, similar to the cathode, the peak around 0 ppm is attributed to Li$^+$ of SEI and the dried electrolyte salt. However, the line-widths are much larger than the corresponding ($\sim$ zero ppm) part in the cathodes. Although the cells are assumed to be fully discharged, the weak peak around 45ppm of FP03 is indicative of a small amount of intercalated lithium[22]. The overlapped peak around 8ppm might be a contribution from a different phase of intercalated lithium[22].

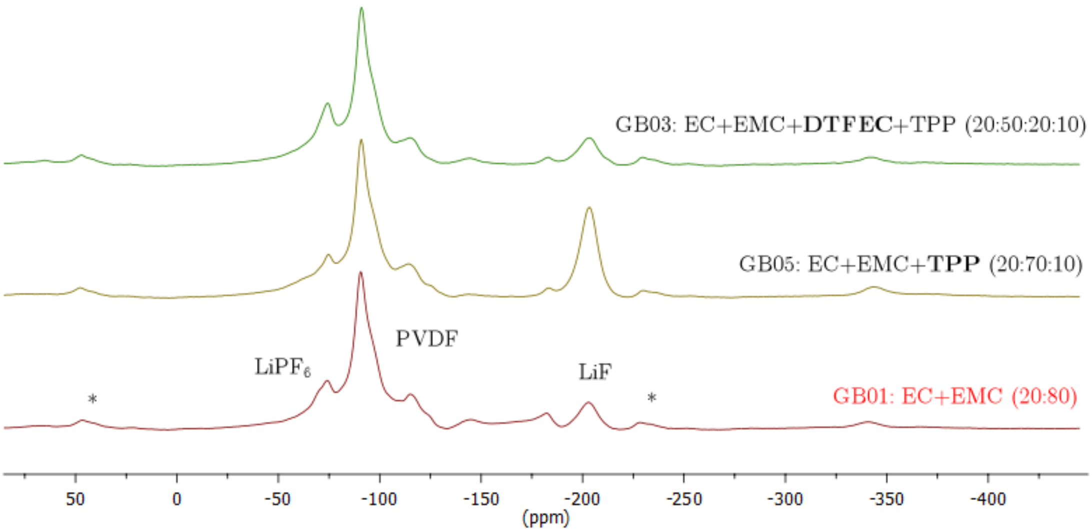

Figure 7.3.5: ^{19}F MAS NMR spectra of the cathode GB series.

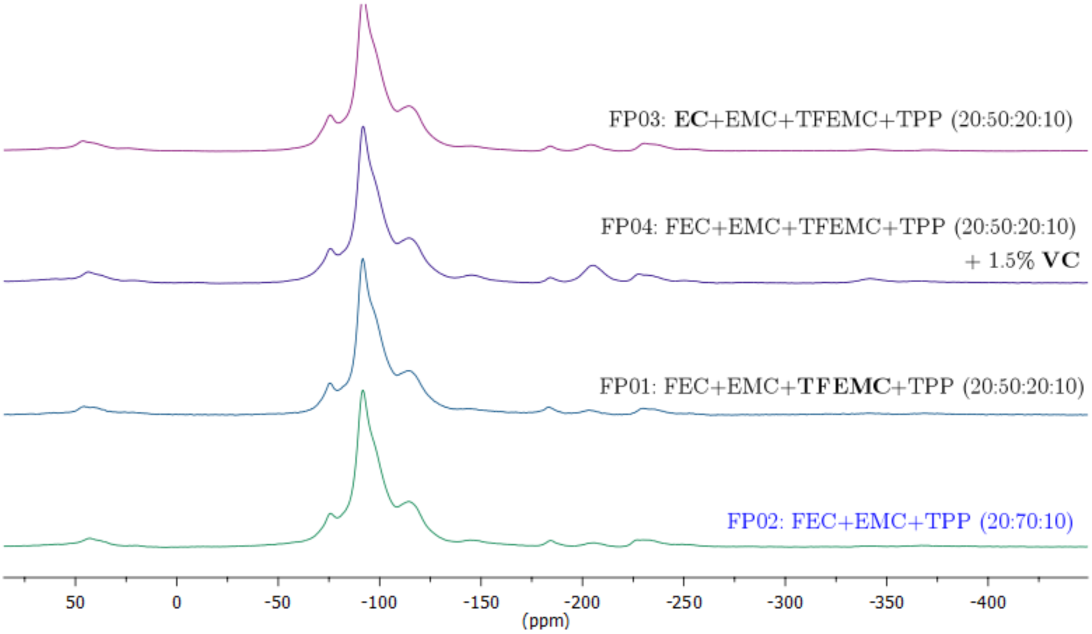

Figure 7.3.6: ^{19}F MAS NMR spectra of the cathode FP series.

^{19}F MAS NMR of the GB and FP cathode series are illustrated in Fig. 7.3.5 and 7.3.6 respectively. These data appear very similar, yet there are notable differences. The peaks around -75 ppm and -205ppm are assigned to LiPF$_6$[22, 23] in the dried electrolyte and LiF[22] respectively. The resonances of PVDF, which is used as a binder, appears around -90ppm and -113ppm[22]. All ^{19}F spectra are normalized to the PVDF peak intensity at -90ppm. The weak cathode peak, around

-184ppm is in the region of covalent CF but is presently unassigned. Apparently the main difference between these two sample groups is that the GB series contains significantly higher LiF and $LiPF_6$ contents than the FP series.

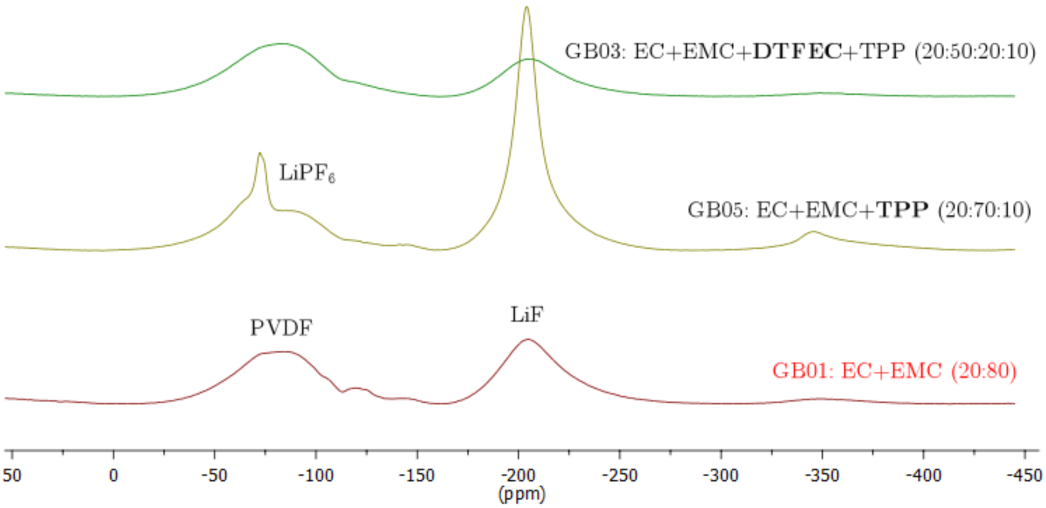

Figure 7.3.7: ^{19}F MAS NMR spectra of the anode GB series.

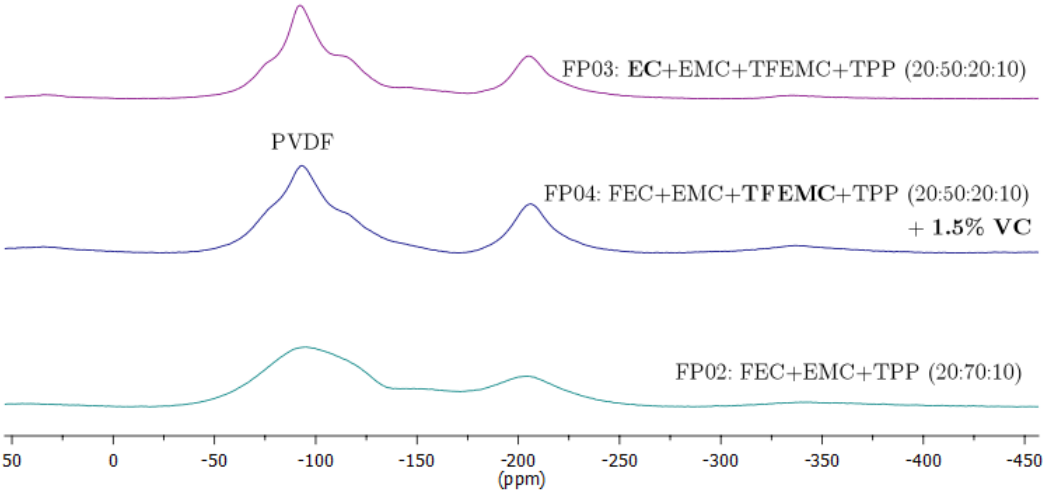

Figure 7.3.8: ^{19}F MAS NMR spectra of the anode FP series.

^{19}F MAS NMR of the GB and FP series anodes are illustrated in Fig. 7.3.7 and 7.3.8 respectively. The $LiPF_6$ peak, still observed around -75ppm along with the PVDF peaks around -90ppm and -113ppm, are considerably weaker than those for the cathode. This may be due to both the use of less binder in the anode and better rinsing efficiency for the anodes after harvesting them. However, in general, the spectra indicate that the anodes maintain a higher LiF concentration than the cathodes which is particularly true for sample GB05: 1.00 M LiPF6 EC+EMC+TPP (20:70:10 v/v %).

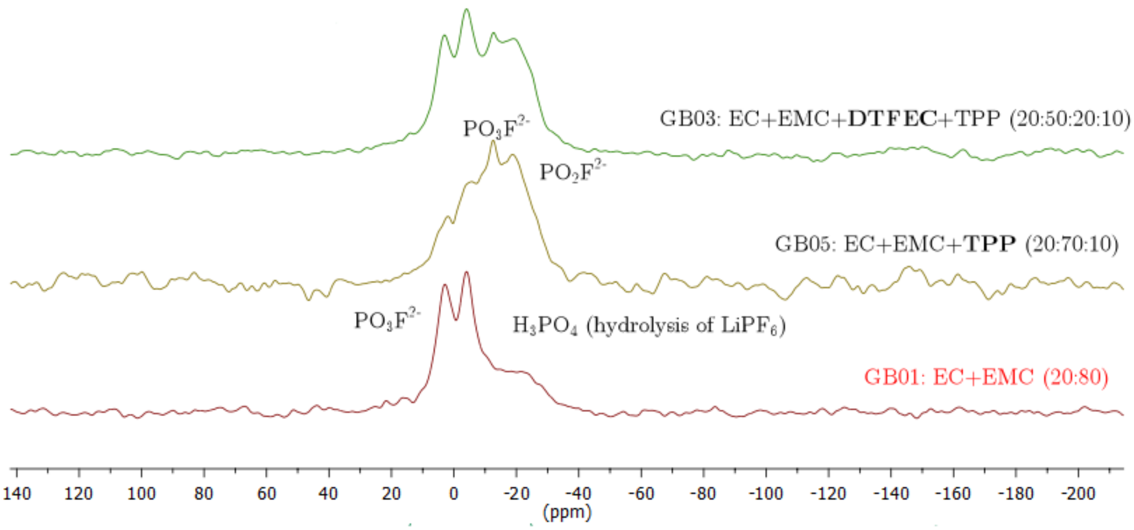

Figure 7.3.9: ^{31}P MAS NMR spectra of the cathode GB series.

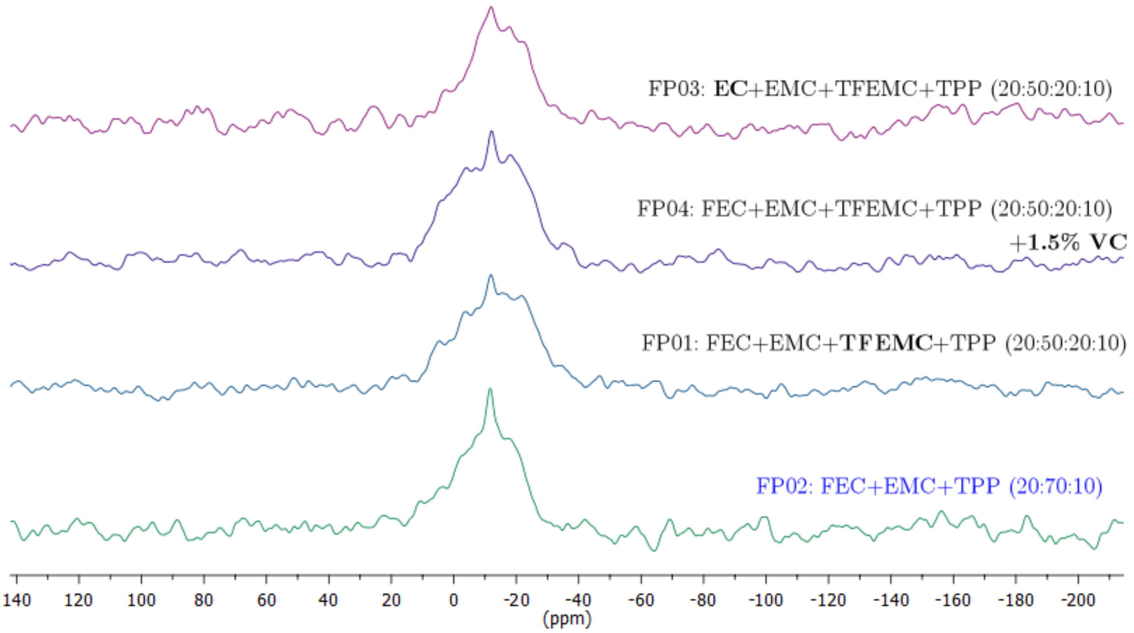

Figure 7.3.10: ^{31}P MAS NMR spectra of the cathode FP series.

^{31}P MAS NMR of the GB and FP cathode series are illustrated in Fig. 7.3.9 and 7.3.10 respectively. Although samples were run a long period of time the SNR is very low. However four resolvable peaks can be identified at 4, -4, -12 and -18ppm. The peak at 4ppm may be assigned to H_3PO_4 as a result of the hydrolysis of $LiPF_6$[23]. The peaks at -4 and -12ppm are assigned to

PO_3F^{2-} and the peak at -18ppm is assigned to PO_2F^{2-}[23]. No resolved signals were found between -133 and -156 ppm for PF_6^-. This is consistent with the absence of the corresponding ^{19}F peaks in these samples. Beyond these ^{31}P resonances, additional spectral features imply the presence of phosphorus based additives (previously mentioned). In this regard, The individual NMR studies of the phosphorus additives such as TPP would help identify the spectral features associated with the additives.

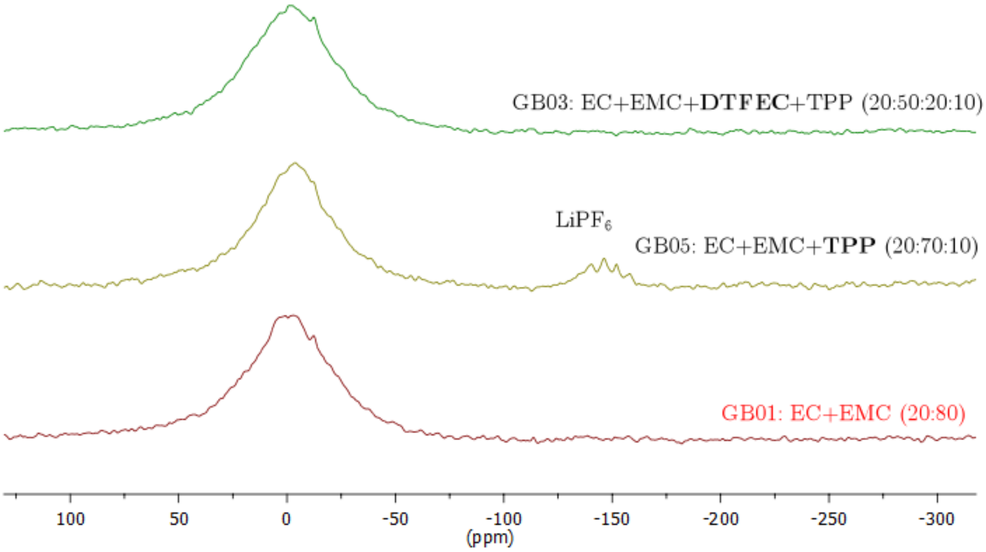

Figure 7.3.11: ^{31}P MAS NMR spectra of the anode GB series.

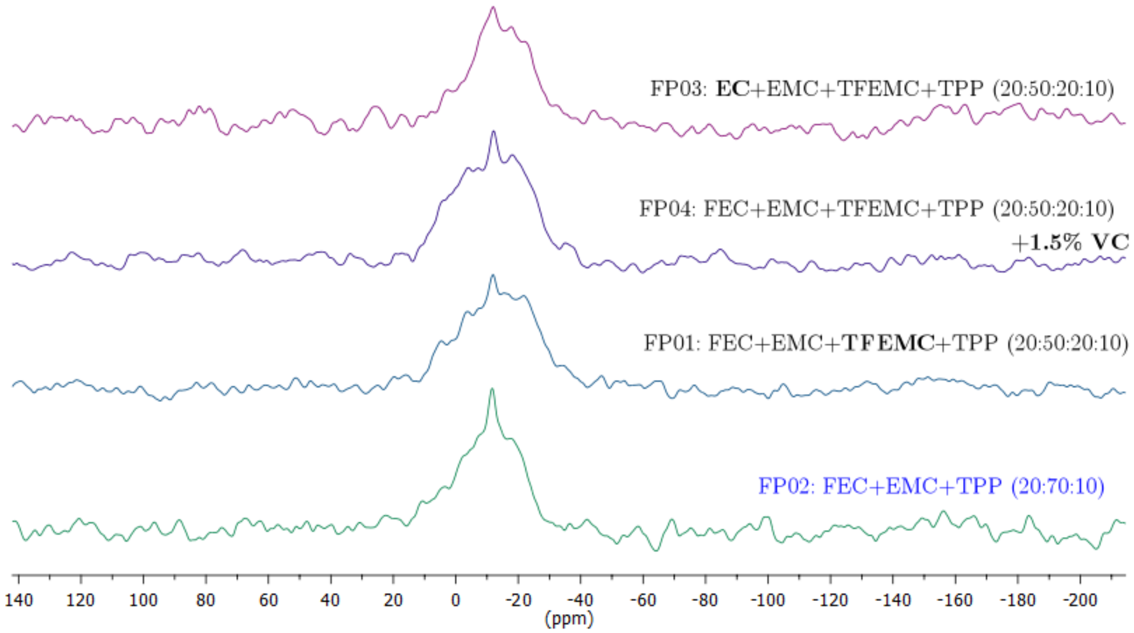

Figure 7.3.12: ^{31}P MAS NMR spectra of the anode FP series.

^{31}P MAS NMR of the GB and FP cathode series are illustrated in Fig. 7.3.11 and 7.3.12 respectively. Based on line-width, the anode spectra display a more disordered nature of the various separate phosphate peaks observed for the cathodes, only the PO_3F^{2-} peak at 12ppm is resolvable; the other peaks overlap within the broad feature. A set of features around 150ppm appeared only in the GB05 sample: 1.00 M LiPF6 EC+EMC+TPP (20:70:10 v/v %) and was assigned to PF_6^-[23], in support of our interpretation for the ^{19}F spectra illustrated in Fig. 7.3.7.

7.4 Conclusions

This is an ongoing project, and NMR studies of only two sample sets have been completed. Although the results are too preliminary for a definitive conclusion, some interesting observations have been noted. Moreover GB05 sample was significantly different from the other by having considerably higher PF_6^- present. Also GB03 showed the highest Ni^{3+}/Ni^{4+} ratio among the others. Although the different chemical shifts were observed, the correlation between the intensities and the additive amounts are not clear. The individual samples of additives such as TPP were requested and manual mixtures of them with known quantities should be investigated as the next step.

Bibliography

[1] Levitt, Malcolm H. Spin Dynamics - Basics of Nuclear Magnetic Resonance. John Wiley & Sons, Ltd, 2005.

[2] Hornak, Joseph P. The Basics of NMR, http://www.cis.rit.edu/htbooks/nmr. 1997-2008.

[3] MacDougall F, Ennis J, Cooper R, Bates J and Seal K. High energy density pulsed power capacitors. IEEE, 1 (2003), 513-7.

[4] He X, Yao K and Gan B. Phase transition and properties of a ferroelectric poly(vinyldene fluoride-hexafluoropropylene) copolymer. J. Appl. Physcs., 97 (2005), 084101.

[5] Reddy T.B, Handbook of Batteries, 4th ed., McGraw-Hill, New York, 2010.

[6] Leifer N.D, Johnson V.S, Ben-Ari R, Gan H, Lehnes J.M, Guo R, Lu W, Muffiletto BC, Reddy T, Stallworth P.E, Greenbaum S.G, J. Electrochem. Soc. 157 (2010) A148–A154.

[7] Thomas R, Krawietz, James F, Chem. Commun. (1998) 2151–2152.

[8] Giraudet J, Dubois M, Guerin K, Hamwi A, Masin F, J. Phys. Chem. Sol. 67 (2006) 1100–1105.

[9] Giraudet J, Dubois M, Guerin K, Delabarre C, Pirotte P, Hamwi A, Masin F, Sol. State NMR 31 (2007) 131–140.

[10] Dubois M, Guerin K, Pinherio J.P, Fawal Z, Masin F, Hamwi A, Carbon 42 (2004) 1931–1940.

[11] Chang W.K, Liao M.Y, and Gleason K.K, Characterization of Porous Silicon by Solid-State Nuclear Magnetic Resonance. J. Phys. Chem, 100 (1996), 19653-19658.

[12] Pietra T, Bifone A, Roth R.D, Koch V.P, Alivisatos A.P, Pines A. ^{29}Si high resolution solid state nuclear magnetic resonance spectroscopy of porous silicon. Journal of Non-Crystalline Solids, 202 (1996), 68-76.

[13] Klinowski, Sean A. Axon and Jacek. Solid-State NMR Studies of Zeolite [Si,B]-ZSM-5 Synthesized by the "Fluoride Method". J. Phys. Chem., 98 (1994), 1929-1932.

[14] Kim Y, Kirkpatrick R.J. ^{11}B NMR investigation of boron interaction with mineral surfaces: Results for boehmite, silica gel and illite. Geochimica et Cosmochimica Acta, 70 (2006), 3231-3238.

[15] Franke D, Hudalla C, Maxwell R, and Eckert H. ^{31}P-^{113}Cd and ^{31}P - ^{29}Si CP/MAS-NMR in Inorganic Semiconductors. J. Phys. Chem., 96 (1992), 7506-7509.

[16] Butturi M.A, Carotta M.C, Martinelli G, Passari L, Youssef G.M, Chiorino A and Ghiotti G, Effects of ageing on porous silicon photoluminancence: Correlation with FTIR and UV-VIS spectra, Solid state Commun, Vol 101, pp. 11-16, 1997

[17] Battery statistics, BatteryUniversity.com.

[18] Nine-volt battery, http://en.wikipedia.org/wiki/Nine-volt_battery.

[19] Thackeray M.M, Thomas J.O, and Whittingham M.S. Science and Applications of Mixed Conductors for Lithium Batteries. Materials Research Society, March 2000.

[20] Mackey M, Hiltner A, Baer E, Flandin L, Wolak M.A and Shirk J.S, Enhanced breakdown strength of multilayered films fabricated by forced assembly microlayer coextrusion. J. Phys. D: Appl. Phys. 42 (2009) 175304 (12pp)

[21] Zlatic V and Hewson A.C, Properties and Applications of Thermoelectric Materials. Springer, 2008

[22] Meyer BM, Leifer N, Sakamoto S, Greenbaum S.G and Grey C.P, High Field Multinuclear NMR Investigation of the SEI Layer in Lithium Rechargeable Batteries. Electrochemical and Solid-State Letters (2005), A145-A148

[23] Plakhotnyk A.V, Ernst L and Schmutzler R, Hydrolysis in the system $LiPF_6$ — Propylene carbonate — Dimethyl carbonate - H_2O. Journal of Fluorine Chemistry 126 (2005) 27–31